American Mineralogist, Volume 110, pages 1574–1596, 2025

Snowball quartz in highly fractionated peraluminous granites: An indicator of multiple magma degassing

Daohan Zhang[1,2,*], Kunfeng Qiu[3,†], Chang Xu[4], Yuwei Luan[2], Yanjun Li[2], Junhao Wei[2], and Jun Deng[3]

[1]State Key Laboratory of Critical Mineral Research and Exploration, Institute of Geochemistry, Chinese Academy of Sciences, Guiyang 550081, China
[2]School of Earth Resources, State Key Laboratory of Geological Processes and Mineral Resources, China University of Geosciences, Wuhan 430074, China
[3]School of Earth Sciences and Resources, China University of Geosciences, Beijing 100083, China
[4]School of Earth Sciences, China University of Geosciences, Wuhan 430074, China

Abstract

Snowball quartz is commonly found in highly fractionated peraluminous granites that may be associated with mineralization of Ta, Nb, Li, W, Sn, and Rb. The genesis of snowball quartz has been a subject of controversy, and its genetic relationship with potential rare metal mineralization remains poorly understood. This work presents a study of the mineralogy and chemistry of quartz and plagioclase from the Yashan pluton in southern China. The Yashan pluton hosts the Yichun Ta-Nb-Li deposit and is primarily composed of two-mica granite, Li-mica granite, and topaz-lepidolite granite, which were intruded by granite dikes. The texture known as "snowball" is observed in quartz from Li-mica granite, but it is more frequently and prominently developed in quartz from topaz-lepidolite granite and granite dikes. This texture is characterized by the zonal arrangement of prismatic albite (referred to as snowball albite) within quartz phenocrysts, with the {010} face of snowball albite preferentially adhering to the crystal faces of quartz. It typically develops in specific domains of the mantle and/or rim of quartz phenocrysts, and occasionally in their cores. The snowball texture is preferentially developed on the prism faces (*m*) of quartz, as indicated by a higher abundance of snowball albites on these faces compared to others. The snowball-textured quartz domain (SBTQD) is texturally similar to other domains from the same growth zone and chemically overlaps with magmatic quartz cores or rims. The snowball albites are chemically indistinguishable from magmatic albite inclusions entrapped within quartz cores. These pieces of evidence suggest that the SBTQDs have a magmatic origin. Given the specific morphologies of snowball quartz (well development of prism faces) and albite (prismatic with a high aspect ratio of ~5–10), along with the development of sector zoning in quartz, it is proposed that the snowball quartz formed as a result of rapid growth of quartz and albite under moderate undercooling (ΔT = 50–100 °C) at near-solidus conditions, which was associated with multiple episodes of magma degassing. From the perspective of Ta-Nb mineralization, this degree of undercooling would significantly reduce the solubility of tantalite by more than 70–90%, thereby facilitating its crystallization. This process also promotes the further crystallization of already saturated columbite. Therefore, snowball quartz could serve as an exploration indicator for Ta-Nb deposits associated with highly fractionated peraluminous granites.

Keywords: Snowball quartz, Yichun 414 deposit, Yashan pluton, Ta-Nb mineralization, undercooling, magma degassing

Introduction

Snowball quartz is a distinctive type of quartz characterized by a paragenetic texture that features a concentric arrangement of mineral inclusions, predominantly consisting of albite, along with rare occurrences of K-feldspar, mica, zircon, and apatite (Müller and Seltmann 1999; Müller et al. 2009; Schwartz 1992). This variety of quartz is typically found at the apex of highly fractionated aluminous (peraluminous and metaluminous) granites, many of which are associated with rare metal mineralization (e.g., Sn, W, Nb, Ta, Li, and Rb; Table 1) (Marignac et al. 2020; Michaud and Pichavant 2020; Müller et al. 2018; Müller and Seltmann 1999; Wu et al. 2018). The potential genetic relationship between the formation of snowball quartz and rare metal mineralization remains poorly understood (e.g., Müller and Seltmann 1999), as the genesis of quartz with such a peculiar texture is still a subject of debate. Many studies agree that snowball quartz is magmatic in origin and crystallized simultaneously with albite from either a normally cooling magma (Pollard 2021; Yin et al. 1995) or from a degassed magma (Müller and Seltmann 1999; Müller et al. 2009; Wang et al. 2019). In contrast, several studies have instead interpreted snowball quartz as having been formed through the hydrothermal replacement of albite and lepidolite (e.g., Wu et al. 2017, 2018).

* Corresponding author E-mail: zhangdh@cug.edu.cn, zhangdaohan@mail.gyig.ac.cn Orcid https://orcid.org/0000-0002-7788-4591
† Orcid https://orcid.org/0000-0002-3185-9446

Table 1. Occurrence of snowball quartz in highly evolved aluminous granites and related mineralization

Location	Name of pluton	Granite type	Mineralization type	Reference
Eastem Erzgebirge, Germany	Schellerhau	Albite granite (SG3)	Sn	Müller and Seltmann (1999); Müller et al. (2000)
Itu Rapakivi Province, Brazil	Correas	Topaz-muscovite-albite granite	Sn	Bettencourt et al. (2005)
Goiás, Brazil	Boa Vista and Pelotas	Albitite	Sn	Sirqueira et al. (2018)
Inner Mongolia, China	Weilasituo	Quartz porphyry	Sn, W, Li	Gao et al. (2024)
German-Czech border	Cínovec/Zinnwald	Zinnwaldite granite	Sn, W, Li	Breiter et al. (2017); Müller et al. (2018)
Alaska, USA	Kougarok	Zinnwaldite granite	Sn, Ta, Li	Soloviev et al. (2020)
Czech-Bavarian border	Rozvadov	Albite-zinnwaldite topaz granite	Sn, Nb, Ta	Breiter and Siebel (1995); Breiter et al. (2013)
Krušné Hory, Czech Republic	Podlesí	Albite-zinnwaldite-topaz granite	Sn, W, Nb, Ta	Müller and Seltmann (1999); Breiter et al. (2005)
Beira Baixa, Portugal	Panasqueira	Albite-Li-muscovite granite	W, Sn, Cu	Marignac et al. (2020)
Hunan Province, China	Laiziling	Albite granite	W, Nb, Ta	Xie et al. (2018)
Jiangxi Province, China	Dajishan	Muscovite albite leucogranite	W, Ta, Nb	Wu et al. (2017)
Central Eastern Desert, Egypt	Um Naggat	Albite granite	Nb, Ta	Gamal-Adeen et al. (2023)
Central Eastern Desert, Egypt	Nuweibi	Albite granite	Nb, Ta	El-Dokouny et al. (2023)
Jiangxi Province, China	Songshugang	Topaz K-feldspar granite	Nb, Ta, W, Sn	Zhu et al. (2024)
Inner Mongolia, China	Jiabusi	Li-mica albite granite	Ta, Nb	Zhang et al. (2022a)
Jiangxi Province, China	Yashan	Topaz-lepidolite granite	Ta, Nb, Li	Schwartz (1992); Yin et al. (1995)
Guangxi Province, China	Limu	Topaz-albite granite	Ta, Nb, Sn, W	Zhu et al. (2001)
Eastern Desert, Egypt	Nuweibi	Li-albite granite	Ta, Nb, Be, Sn	Abdalla (2009)
Eastern Desert, Egypt	Abu Dabbab	Li-albite granite	Ta, Nb, Be, Sn, W	Abdalla (2009)
Midyan, Saudi Arabia	Jabal Tawlah	Albite granite	Ta, Nb, Y, Zr, Th, Sn	Gahlan et al. (2022)
Eastern Desert, Egypt	Mueilha	Albite granite	Ta, Sn, W	Seddik et al. (2020)
Barco e Coutada, Portugal	Argemela	Albite granite	Li, Sn, Nb, Ta, W	Michaud et al. (2020)
Xinjiang Province, China	Baishitouquan	Topaz- and amazonite-bearing leucogranite	Rb	Wu et al. (2011)
Inner Mongolia, China	Shihuiyao	Amazonite-bearing granite	Rb, Nb, Ta	Sun et al. (2023)

Among the related types of rare metal mineralization, Nb-Ta mineralization is characterized by disseminated columbite-tantalite, microlite, and Ta-rich cassiterite found in the cupola of highly differentiated peraluminous granites (Linnen and Cuney 2005). This type of deposit serves as a significant source for the global supply of Ta and Nb metals (Jiang et al. 2023; Linnen et al. 2014; Wang et al. 2020). However, there is no consensus regarding the enrichment mechanisms of these metals. Numerous studies suggest that the primary Nb-Ta-bearing minerals are magmatic in origin and formed as a result of extensive fractionation (Linnen and Cuney 2005; Linnen et al. 2014; López-Moro et al. 2017; Yin et al. 2022). Conversely, some studies propose that tantalite and microlite mainly formed during post-magmatic metasomatic processes (e.g., Gahlan et al. 2022; Seddik et al. 2020; Wu et al. 2018). The fundamental argument for this interpretation is based on the metasomatic origin of snowball quartz (Wu et al. 2017, 2018). Therefore, elucidating the origin of snowball quartz is a crucial step toward understanding the enrichment mechanisms of Nb and Ta in highly evolved peraluminous granites. This may also provide petrological insights into the associated W-Sn±Li±Rb mineralization.

This work presents a comprehensive study of the texture and chemistry of quartz from the Yashan pluton, which hosts the Yichun Ta-Nb-Li deposit in southern China (Wu et al. 2018; Yin et al. 1995). Snowball quartz grains are found in late evolved Li-mica granite, topaz-lepidolite granite, and granite dikes from the Yashan pluton. The quartz crystals from different granite types, along with the spatially and genetically associated plagioclase, reveal the existence of two separate magma chambers that fed the Yashan pluton. The magmatic origin of snowball quartz has been confirmed, and the potential processes responsible for its formation have been discussed. This discovery has significant implications for rare metal mineralization and mineral exploration. Additionally, it is important to note that the snowball texture discussed in this study refers specifically to that found in highly fractionated granites, rather than the texture observed in garnet from shear zones, which is clearly of metamorphic origin (e.g., Robyr et al. 2009; Williams and Jiang 1999).

Geological Background and Sample Information

Geology of the Yashan pluton

The Cathaysia Block in southern China hosts extensive Nb-Ta mineralization that developed during the late Jurassic, with subordinate mineralization occurring in the late Silurian to middle Devonian, Triassic, and Cretaceous periods (Che et al. 2019). The Yashan pluton is located near the northwest border of the Cathaysia Block, ~20 km southeast of Yichun City in Jiangxi Province. It is a composite, vertically zoned peraluminous granite pluton that intruded the late Neoproterozoic metasediments of the Banxi Group, which consist of metasandstones, slate, schist, and phyllite (Yin et al. 1995). This pluton comprises, from early to late, two-mica granite, Li-mica granite, topaz-lepidolite granite, and marginal pegmatite [also known as stockscheider, characterized by the K-feldspar-dominated unidirectional solidification texture (UST) zones] (Breiter et al. 2005; Schwartz 1992). The two-mica (muscovite and protolithionite) granite is volumetrically dominant, occupying about 60% of the Yashan pluton's outcrop, and gradually evolved to muscovite granite toward its margin (Yin et al. 1995). This granite was intruded and overlain by Li-mica granite, which exhibits a fine-grained texture at its contact (Yin et al. 1995). The Li-mica granite was subsequently intruded by, or gradually evolved upwards to, the topaz-lepidolite granite, a relationship that remains contentious due to the ambiguity regarding their contact (Pollard 2021; Yin et al. 1995). The topaz-lepidolite granite has a thin aplitic margin at its apex, which is separated from the overlying metasediments by the stockscheider (Pollard 2021; Yin et al. 1995). These granitic lithologies were later intersected by northwest- and northeast-trending granite dikes

(Fig. 1a). The topaz-lepidolite granite serves as the primary host for the Ta-Nb-Li orebody, characterized by disseminated columbite group minerals, microlite, Ta-rich cassiterite, and lepidolite throughout the rock (Yin et al. 1995). The Li-mica granite, along with the granite dikes, is currently being exploited for these metals due to their increasing economic significance. Although a broad range of emplacement ages, varying from 161 to 150 Ma, have been reported for the Yashan pluton based on zircon U-Pb (Li 2015; Lou et al. 2005; Yang et al. 2014), columbite-tantalite U-Pb (Che et al. 2019), and molybdenite Re-Os (Li 2015; Zhang et al. 2019) dating methods, the most recent U-Pb dating of magmatic cassiterites from the Li-mica granite, topaz-lepidolite granite, and granite dikes suggests that the Yashan pluton was most likely emplaced at 148–150 Ma (Zhang et al. in revision).

A late, concealed muscovite granite stock was discovered intruding the two-mica granite in the northwest part of the Yashan pluton (Fig. 1). The upper portion of this stock is composed of porphyritic muscovite granite, which contains xenoliths of two-mica granite near the contact zone (Yin et al. 1995). The porphyritic muscovite granite is separated from a medium-grained muscovite granite below by a marginal stockscheider (Yin et al. 1995). The latter was associated with the formation of wolframite-quartz veins that extend to the present surface (Figs. 1a and 1b). These muscovite granites primarily consist of K-feldspar, plagioclase, quartz, and muscovite (Pollard 2021; Yin et al. 1995). They are believed to have evolved independently from the Yashan pluton due to their distinct chemical composition compared to the overlying two-mica granite (Yin et al. 1995).

Sample information

Samples of different rock lithologies from the Yashan pluton, excluding the stockscheider, were collected, and their locations are depicted in Figure 1a. All samples are identical to those described in Zhang et al. (in revision). The two-mica granite (sample YS06) displays a medium- to coarse-grained texture and comprises 35–40 vol% quartz, 30–35 vol% K-feldspar, 25–30 vol% plagioclase, and ~5 vol% mica, along with minor accessory minerals including apatite, fluorite, garnet, ilmenite, rutile, titanite, and zircon (Figs. 2a and 3a). The micas in this rock are predominantly protolithionite, with subordinate muscovite (Li et al. 2015); the latter is typically anhedral, either overgrowing on protolithionite or occurring interstitially with protolithionite, feldspars, and quartz (Fig. 3a). The Li-mica granite (sample YS04) is medium-grained and consists of quartz (35–40 vol%), K-feldspar (20–25 vol%), plagioclase (20–25 vol%), and Li-mica (10–15 vol%; primarily Li phengite and Li muscovite; Li et al. 2015), with cassiterite, columbite-tantalite, apatite, beryl, fluorite, topaz, and zircon as accessory minerals (Figs. 2b and 3b). Both quartz and K-feldspar in this rock exhibit the snowball textures, as evidenced by many albite inclusions aligned along their growth zones (Figs. 2b and 3b). The topaz-lepidolite granite (sample YS01) features a porphyritic texture and consists of quartz, K-feldspar, and topaz as phenocrysts embedded in a medium- to fine-grained groundmass of albite, lepidolite, quartz, and topaz (Figs. 2c and 3c). In addition to quartz and K-feldspar, the topaz phenocryst in this rock also displays a snowball texture (Pollard 2021; Wu et al. 2018). Accessory minerals present in the topaz-lepidolite granite include amblygonite, beryl, cassiterite, columbite-tantalite, and zircon (Fig. 2c). The late granite dike (sample YS03) is porphyritic and consists of phenocrysts of petalite, K-feldspar, and quartz set in a fine-grained groundmass of quartz, albite, lepidolite, and topaz, with accessory minerals including amblygonite, apatite, beryl, cassiterite, and columbite-tantalite (Figs. 2d and 3d). The snowball texture is developed in K-feldspar and quartz phenocrysts, but not in petalite (Figs. 2d and 3d).

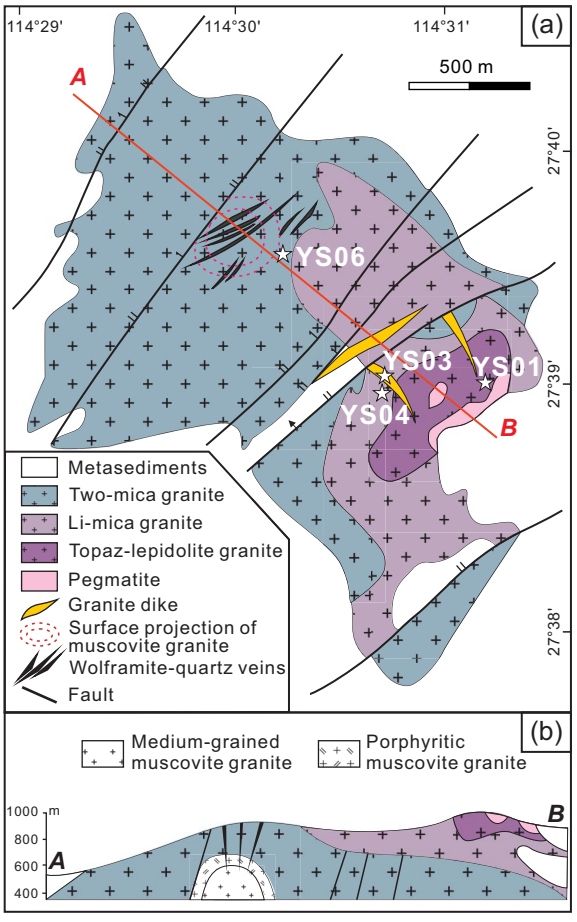

Figure 1. (**a**) A simplified geological map of the Yashan pluton, illustrating the distribution of different rock lithologies, the locations of samples, and the cross section depicted in (**b**) [modified after Yin et al. (1995)]. (**b**) A cross-sectional sketch demonstrating the vertical distribution of different granite types and the concealed porphyritic to medium-grained muscovite granite stock [modified after Yin et al. (1995)]. (Color online.)

Methods

The polished rock sections, with a thickness ranging from 100 to 300 μm, were initially examined under a microscope equipped with an LED light source to select representative quartz grains from each granite for subsequent measurements.

TIMA microanalyses

A TESCAN Integrated Mineral Analyzer (TIMA) in the Collaborative Innovation Center for Exploration of Strategic Mineral Resources at the China University of Geosciences (Wuhan) was utilized for automated mineralogical, modal, and textural analyses. The TIMA measurements were conducted at 25 kV and 8nA, with a working distance of 15 mm and a pixel size of 3 μm, using the dot-mapping mode. The current and backscattered electron (BSE) signal strengths were calibrated using a platinum Faraday cup automatic program, while the energy-dispersive spectroscopy (EDS)

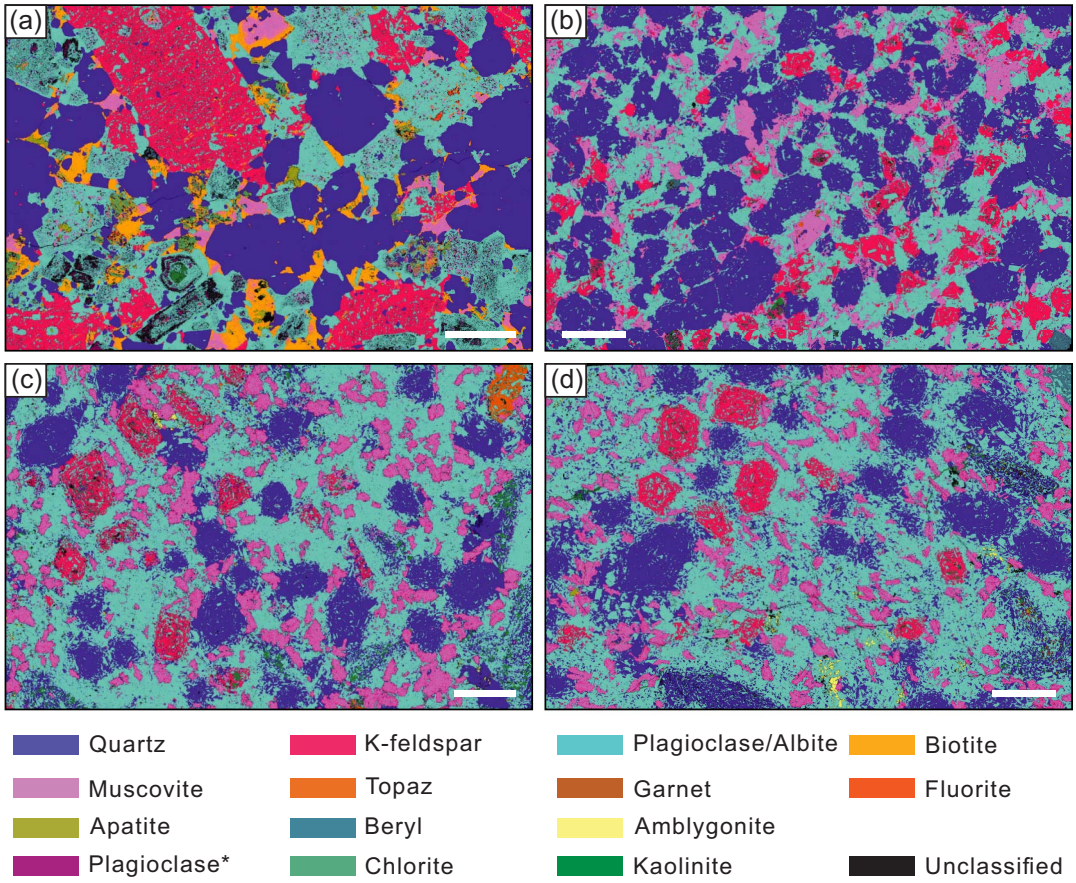

Figure 2. TIMA mineral maps of thick sections of various granite types from the Yashan pluton. (**a**) Two-mica granite (YS06); (**b**) Li-mica granite (YS04); (**c**) topaz-lepidolite granite (YS01); (**d**) granite dike (YS03). Plagioclase* in the legend represents the altered domain of plagioclase from the two-mica granite. Muscovite refers to muscovite in (**a**), to Li phengite and Li muscovite in (**b**), and to lepidolite in (**c**) and (**d**). Chlorite and kaolinite are hydrothermal minerals that replace the feldspars and micas. The length of the white scale bar in each panel is 5 mm. (Color online.)

signal was calibrated with a manganese standard. The samples were scanned using the TIMA liberation analysis module. The spectroscopic data were matched to mineral definition files, facilitating mineral identification and mapping; the volume and mass ratios of all mineral phases were automatically calculated. Offline processing software TIMA was employed to identify minerals and for data statistics and collation.

Cathodoluminescence imaging

The scanning electron microscope-cathodoluminescence (SEM-CL) imaging of quartz crystals was conducted using a Tescan MIRA3 LM instrument equipped with a CL detector at Nanjing Hongchuang Geological Exploration Technology Service Co. The acceleration voltage and current were set at 15 kV and 1.2 nA, respectively.

Electron backscatter diffraction analysis

The crystallographic orientations of selected snowball quartz crystals were measured using electron backscatter diffraction (EBSD). These measurements were performed with a Zeiss Sigma 300VP field emission scanning electron microscope (FESEM) and an Oxford Instruments Aztec Symmetry EBSD detector at the SEM-EBSD laboratory, School of Earth Sciences, China University of Geosciences, Wuhan. The working conditions were as follows: an accelerating voltage of 20 kV, a spot size of 8–10 µm, a working distance of 15–18.5 mm, a sample tilt angle of 70°, and a low-vacuum mode set to 20 Pa. The diffraction patterns were collected and indexed using the Aztec 6.1 software from Oxford Instruments in automatic mapping mode. More details about the EBSD analytical conditions and data processing procedures can be found in Liu et al. (2021).

Electron probe microanalysis

The major elements of plagioclase were analyzed using a JEOL JXA-8230 electron probe microanalyzer (EPMA) equipped with five spectrometers and TAP, PET, LiF, and LDE1 spectrometer crystals at SampleSolution Analytical Technology (SSAT) Co., Ltd., in Wuhan, China. The analytical conditions were set to 15 kV and 10 nA, with a beam diameter of 5 µm. Each element was measured for 10 s with 5 s allocated for the corresponding background measurement. Standardization was performed using albite (Na), orthoclase (K, Al), quartz (Si), rutile (Ti), olivine (Fe, Mg), chrome diopside (Ca), rhodonite (Mn), apatite (P), topaz (F), tugtupite (Cl), and celestite (Sr).

LA-ICP-MS analysis

The trace element compositions of quartz and plagioclase were measured using a Coherent GeolasHD system equipped with a 193 nm excimer laser coupled to a Perkin Elmer 350× quadrupole ICP-MS at the fluid inclusion LA-ICP-MS lab at Nanjing University. The laser operated at a frequency of 10 Hz and an energy density of 10 J/cm^2 for quartz samples, using beam diameters of 44 and 32 µm, depending on the thickness of the growth zone of interest. For plagioclase, the analytical conditions were also set to 10 Hz, but with an energy density of 6 J/cm^2, employing a beam diameter of 44 µm for most plagioclase samples, except for snowball albite inclusions. In the latter case, smaller beam sizes ranging from 32 to 24 µm were used due to the limited exposure of these inclusions. Detailed operating conditions for the laser ablation system and the ICP-MS instrument are provided in Pan et al. (2019). Analyses of quartz samples were quantified using NIST 610 as an external standard and 100 wt% SiO_2 as an internal standard. The accuracy

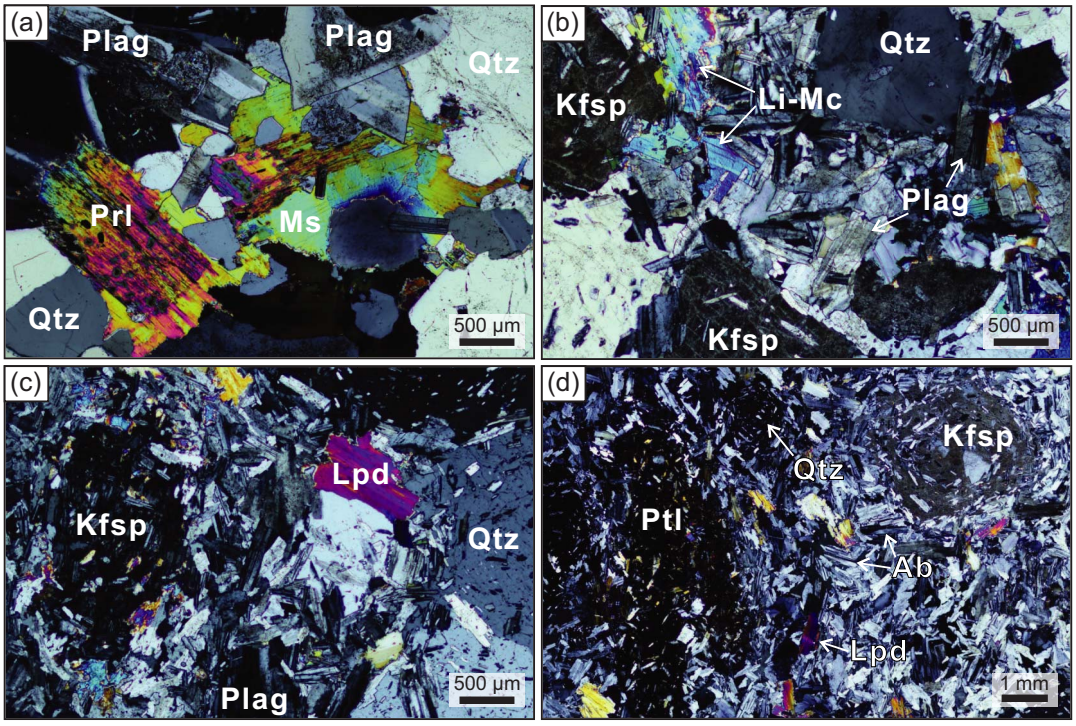

Figure 3. Photomicrographs (under crossed polarizers) of different granitic rocks from the Yashan pluton. (**a**) Two-mica granite (YS06); (**b**) Li-mica granite (YS04); (**c**) topaz-lepidolite granite (YS01); (**d**) granite dike (YS03). Abbreviations: Ab = albite; Kfsp = K-feldspar; Li-Mc = Li-mica; Lpd = lepidolite; Ms = muscovite; Plag = plagioclase; Prl = protolithionite; Ptl = petalite; Qtz = quartz; Tpz = topaz. (Color online.)

of trace element concentrations was periodically checked with the quartz standard described by Audétat et al. (2015). Analyses of plagioclase were quantified using NIST SRM 610 glass as an external standard, followed by normalizing the sum of all major element oxides to 100 wt%.

Results

To prevent any confusion regarding the terminology used in this study, a brief introduction to the snowball texture will be provided before introducing the mineralogy and chemistry of quartz and plagioclase. The chemical compositions of quartz (trace elements) and plagioclase (major and trace elements) are available in Online Materials[1] Tables S1–S3.

As illustrated in Figure 4, the snowball texture is frequently observed in the mantle and/or rim of quartz phenocrysts, indicating that it developed during a specific period of quartz growth. To distinguish it from the other parts of the quartz, the snowball-textured quartz domain (SBTQD) is hereinafter referred to as the specific domain where abundant albite inclusions are aligned parallel to the growth zones of quartz (Fig. 4). These zonally arranged albite inclusions are referred to as snowball albite (Fig. 4), suggesting that they crystallized synchronously with the formation of SBTQDs. In addition to snowball albite, another type of albite inclusion can also be found in snowball quartz. These inclusions are randomly distributed within the core and/or mantle of the quartz phenocrysts and commonly crosscut the quartz growth zones (Fig. 4). This suggests that these inclusions are magmatic albites, which crystallized prior to or concurrently with the quartz core and/or mantle. Therefore, this type of albite will be referred to as magmatic albite inclusion (Fig. 4). Once the growth of snowball quartz ceased, the groundmass quartz and albite would overgrow on its rim during the further cooling of the magma. Such quartz and albite will be referred to as groundmass quartz and groundmass albite, respectively (Fig. 4).

Quartz mineralogy

The medium- to coarse-grained quartz phenocrysts in the two-mica granite predominantly exhibit anhedral to subhedral shapes (Fig. 5), with sizes ranging from 1 to 3 mm. These phenocrysts contain randomly distributed inclusions of feldspar and mica (Fig. 5a). Under the CL imaging, most quartz grains display step zoning, with each growth zone within the interior of the crystal characterized by a rounded or wavy surface (Figs. 5b and 5d). These surfaces have been subsequently overgrown by later generations of quartz, which exhibit either stronger or weaker CL intensity (Figs. 5b and 5d). The groundmass quartz grains are fine-grained and anhedral, potentially displaying concentric growth zoning with indistinct boundaries (Figs. 5c–5d). All quartz crystals in this rock are frequently intersected by late secondary cracks, which have been healed with non-cathodoluminescent quartz (Figs. 5b and 5d).

The quartz phenocrysts in the Li-mica granite are subhedral and may display polyhedral shapes, with rhombohedral faces preferentially developing at one tip (Figs. 6a and 6b). Most grains exhibit a clear core(-mantle)-rim texture under CL imaging. Their cores are CL-bright and show oscillatory zoning, while their rims display lower CL intensity, characterized by weak growth zoning

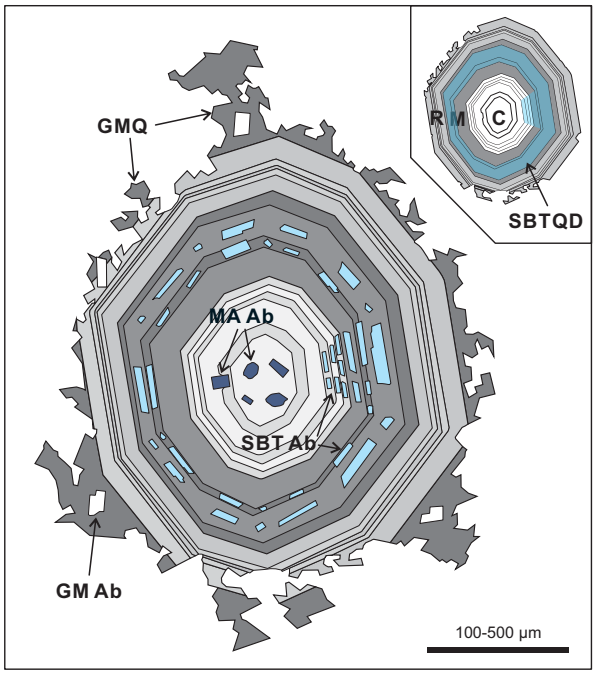

FIGURE 4. A sketch of snowball quartz [modified after Müller et al. (2009)], illustrating the internal texture of the snowball quartz phenocryst, the range of snowball-textured quartz domain (SBTQD), and the occurrence of three types of albite in the rock. Abbreviations: C = core; M = mantle; R = rim; MA Ab = magmatic albite inclusion; SBT Ab = snowball albite; GM Ab = groundmass albite; GMQ = groundmass quartz. (Color online.)

or a homogeneous texture. In some instances, a texturally homogeneous and CL-brighter mantle can be observed overgrowing the oscillatory core (Fig. 6b). The quartz cores commonly contain randomly distributed albite inclusions, whereas their mantles or rims may host several groups of albite that are either scattered or arranged in parallel lines along the quartz growth zone (Figs. 6a, 6b, 6d, and 6e). In the latter case, the zonal distribution of a few albite inclusions outlines a snowball texture, which preferentially develops on rhombohedral faces (Figs. 6b, 6c, 6e, and 6f). The SBTQDs typically show indistinguishable CL responses compared to other domains within the same growth zone (Figs. 6b and 6e). Many quartz phenocrysts display Dauphiné twinning, as indicated by the differing orientations of two sub-crystals in the EBSD pole figures (e.g., Zhao et al. 2013) (Figs. 6c and 6f). The quartz phenocrysts are often overgrown by anhedral groundmass quartz, which exhibits uneven CL intensity (Figs. 6b and 6d). Many quartz grains have been replaced by late hydrothermal quartz, characterized by weak to medium CL intensity (Fig. 6d). Additionally, secondary fractures are prevalent in the quartz crystals from this rock and exhibit dull luminescence (Figs. 6b and 6d).

Quartz phenocrysts from topaz-lepidolite granite are euhedral and show a normal habit characterized by the development of both rhombohedral (*r* and *z*) and prism (*m*) faces (Jovanovski et al. 2022; see Crystal Habits by Amir Chossrow Akhavan, http://www.quartzpage.de/crs_habits.html) (Fig. 7). They display a distinct core-mantle-rim texture and possess a more pronounced snowball texture (Figs. 2c, 7a, and 7d) compared to those found in Li-mica granite. Their cores generally show weak oscillatory zoning and contain scattered albite inclusions (Figs. 7b and 7e). They have resorbed surfaces and are overgrown by a thin layer of mantle, which demonstrates stronger CL intensity and appears texturally homogeneous (Figs. 7b and 7e). In contrast, their rims are oscillatory zoned and display weaker luminescence than the mantle (Figs. 7b and 7e). Abundant zonally arranged albite inclusions are present in these rims (Figs. 7a and 7d), while a few large, lath-like albite inclusions may crosscut the growth zones (Figs. 7a and 7b). These rims transition into a texturally homogeneous groundmass quartz embedded with randomly distributed albite and lepidolite (Figs. 7a, 7b, 7d, and 7e). Occasionally, multiple layers of snowball-textured albite inclusions can also be found within the quartz core, preferentially developing in symmetrical sectors adjacent to the prism faces (Figs. 7a and 7b). They gradually transition into the SBTQD in the rim, where albite layers may envelop the entire growth front of the quartz (Figs. 7a and 7b). Notably, in this instance, the albite inclusions are more abundant on the prism faces than on other faces (Figs. 7a and 7b). In addition, most quartz phenocrysts display Dauphiné twinning (Figs. 7c and 7f), and many also show sector zoning (Figs. 8a–8d). Secondary cracks are significantly less common in quartz phenocrysts from this rock compared to those from Li-mica granite, and no hydrothermal alterations have been observed in these crystals.

The quartz phenocrysts from granite dikes exhibit textural characteristics similar to those of quartz from the topaz-lepidolite granite. These characteristics include the normal habit, well-developed snowball texture (Figs. 9a and 9d), common occurrences of Dauphiné twinning (Figs. 9c and 9f), and sector zoning (Figs. 8e and 8f). However, a notable difference is that nearly all quartz phenocrysts from the dike have undergone extensive alteration, with many parts of the crystals replaced by hydrothermal quartz displaying lower CL intensity (Figs. 9b and 9e).

Quartz chemistry

Quartz phenocrysts from the two-mica granite display overly higher Ti content, and lower Al, Li, and Ge contents, along with lower Ge/Ti and Al/Ti ratios compared to those from the other three granite types (Fig. 10). Many phenocrysts exhibit a rimward increase in Li, Al, and Ge, accompanied by a decrease in Ti (Fig. 5d). Conversely, some phenocrysts may show an abrupt increase in Ti when their cores are overgrown by CL-brighter mantles (Fig. 5b). The groundmass quartz crystals show variable concentrations of Li (54–78 ppm), Al (296–408 ppm), Ti (20–44 ppm), and Ge (0.9–2.7 ppm), which fall within the compositional range of quartz phenocrysts (Fig. 10).

Quartz phenocrysts from Li-mica granite, topaz-lepidolite granite, and granite dikes exhibit similar trace element compositions that overlap with one another (Fig. 10). In general, the core of the quartz phenocryst contains higher concentrations of Al, Ti, and Li, and lower (or comparable) Ge content than the rim (Fig. 10). Consequently, the core exhibits lower Ge/Ti and Al/Ti ratios (Fig. 10d). In contrast, the CL-bright mantle may possess higher concentrations of Al and Li (±Ti) compared to the core (Figs. 6b, 7b, and 7e). The groundmass quartz displays

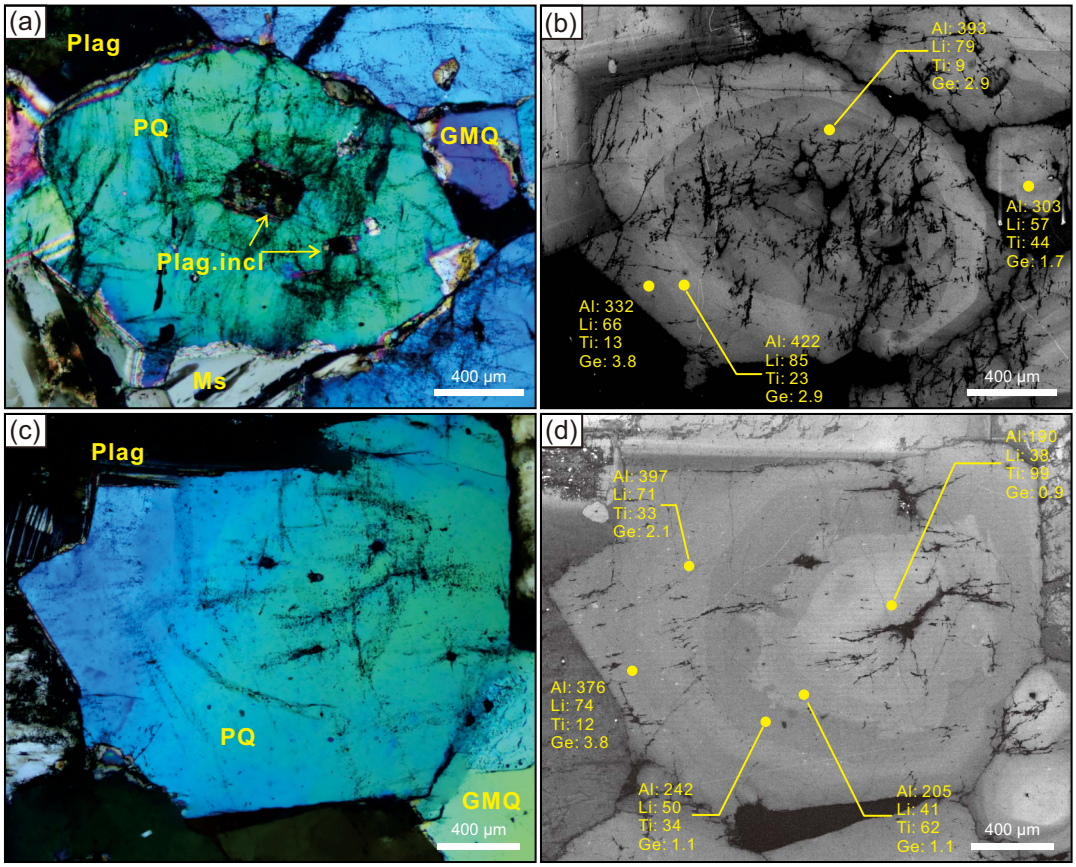

Figure 5. Photomicrographs (**a** and **c**; under crossed polarizers) and cathodoluminescence (CL; **b** and **d**) images of representative quartz crystals from the two-mica granite, showing the internal texture of quartz phenocryst (PQ) and groundmass quartz (GMQ). The yellow circles indicate the locations for LA-ICP-MS trace element analyses, and the corresponding values of selected trace elements (in ppm) are noted alongside. Abbreviation: Plag.incl = plagioclase inclusion. (Color online.)

similar or slightly lower concentrations of Li, Al, Ti, and Ge, along with a slightly higher Ge/Ti ratio than the rim of the quartz phenocryst (Figs. 6, 7, 9, and 10). The late hydrothermal quartz is characterized by high Ge concentrations and variable levels of Li, Al, and Ti (Fig. 10).

The SBTQDs are compositionally similar to neighboring domains within the same growth zone and, in most cases, also to the quartz cores (Fig. 10). In some instances, a compositional trend can be observed from the core through the SBTQDs to the rim (Figs. 11a and 11b). As shown in Figure 11b, except for the interruption of the CL-bright mantle, the concentrations of Al and Li show an overall trend of first increasing (from 607 to 989 ppm and from 131 to 159 ppm, respectively) and then decreasing toward the rim (down to 532 and 99 ppm, respectively; Fig. 11b). However, this trend is not evident in Ge (3.6–4.8 ppm) and Ti (1.1–2.9 ppm) due to their fluctuating contents (Fig. 11b).

Plagioclase mineralogy

The plagioclase phenocrysts in the two-mica granite are subhedral to euhedral and typically range from 2 to 5 mm in size (Figs. 2a and 3a). They frequently exhibit a core(-mantle)-rim texture, as evidenced by the turbid resorption surfaces of the interior domain (Figs. 3a and 12a).

All plagioclases present in Li-mica granite, topaz-lepidolite granite, and granite dikes are nearly pure albite (Fig. 13a; Online Materials[1] Fig. S1). The magmatic albite inclusions can be either anhedral or euhedral; the latter typically display elongated lath- or blade-like shapes and can reach lengths of up to 500–700 μm, with variable aspect ratios of 2.4 to 6.4 (n = 11; Figs. 6a, 7a, 8a, 8d, and 8e). Although these inclusions are entrapped within the quartz core, many are variably altered, particularly those from Li-mica granite and granite dikes, especially when intersected by secondary microcracks (Figs. 6 and 9). Depending on the extent of alteration, they may exhibit a turbid margin or a black mosaic appearance (Figs. 6a, 7d, 9a, 9c, and 12b).

The snowball albites from Li-mica granite, topaz-lepidolite granite, and granite dike commonly exhibit prismatic morphology and are generally smaller in size than magmatic albite inclusions, with lengths usually <300–400 μm (Figs. 7, 9, 11a, and 12c–12g). Most snowball albites from Li-mica granite have low aspect ratios ranging from 2.3 to 5.6 (averaging 3.6; n = 8; Figs. 6a, 6d, and 12c), while those from topaz-lepidolite granite and granite dike display much higher aspect ratios, varying from 4.5 to 9.5 (averaging 6.7; n = 25; Figs. 7a, 7d, 8d, 9a, 9d, 11a, 12b, and 12d–12g). The snowball albites from topaz-lepidolite granite and granite dikes may coexist with lepidolite and columbite group

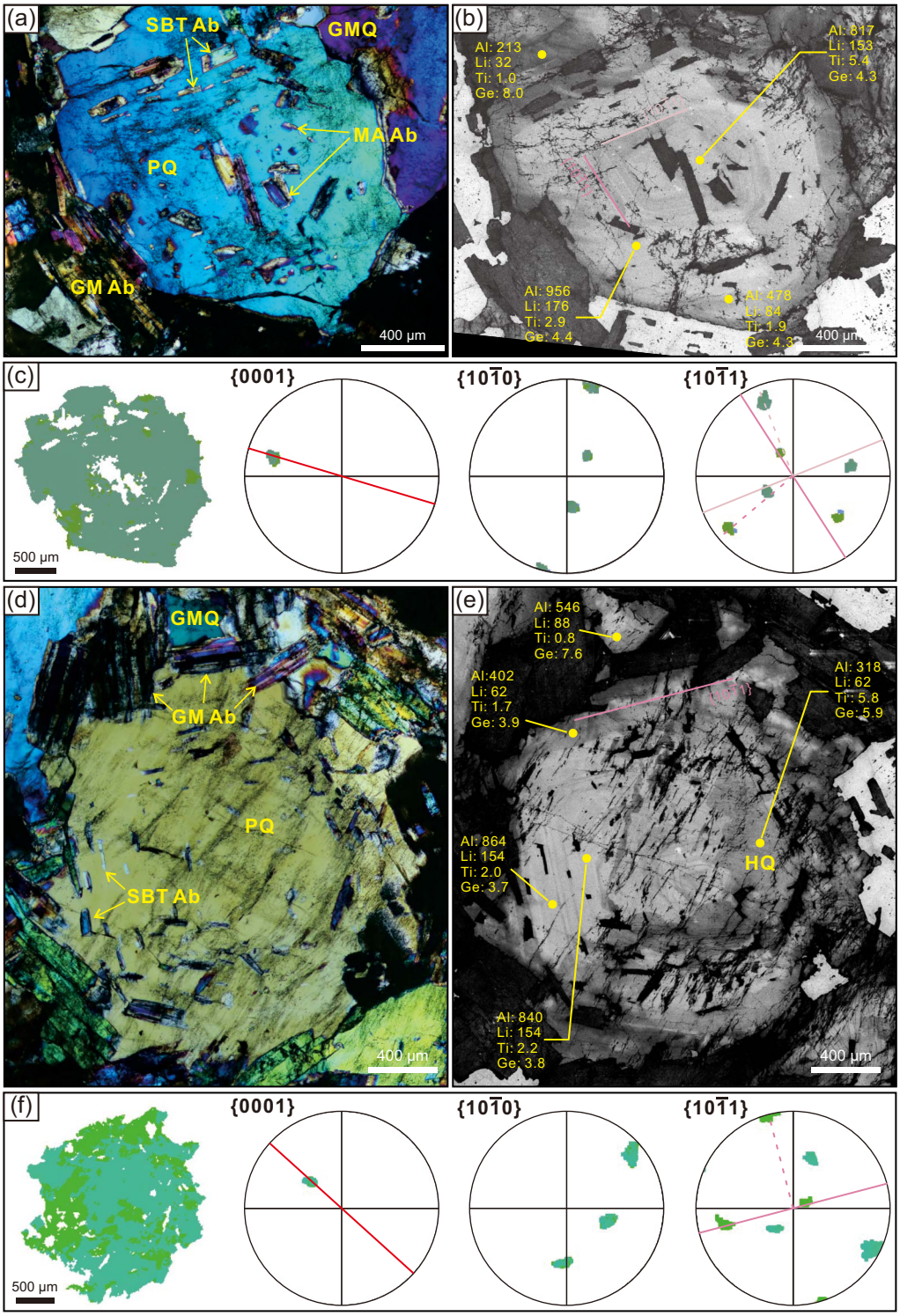

Figure 6. Photomicrographs (**a** and **d**; under crossed polarizers), CL images (**b** and **e**), and EBSD data (**c** and **f**) of representative quartz crystals from Li-mica granite, showing the weak development of snowball texture on the rhombohedral faces (e.g., {10$\bar{1}$1}), and the subsequent alteration of hydrothermal quartz (HQ). Quartz orientation maps (the leftmost panels; all Euler) in (**c**) and (**f**) show the Dauphiné twinning, with different crystals represented by distinct colors. The same color scheme is applied to the corresponding pole figures (the three panels on the right) in (**c**) and (**f**). The concentrations of selected trace elements are given in ppm. (Color online.)

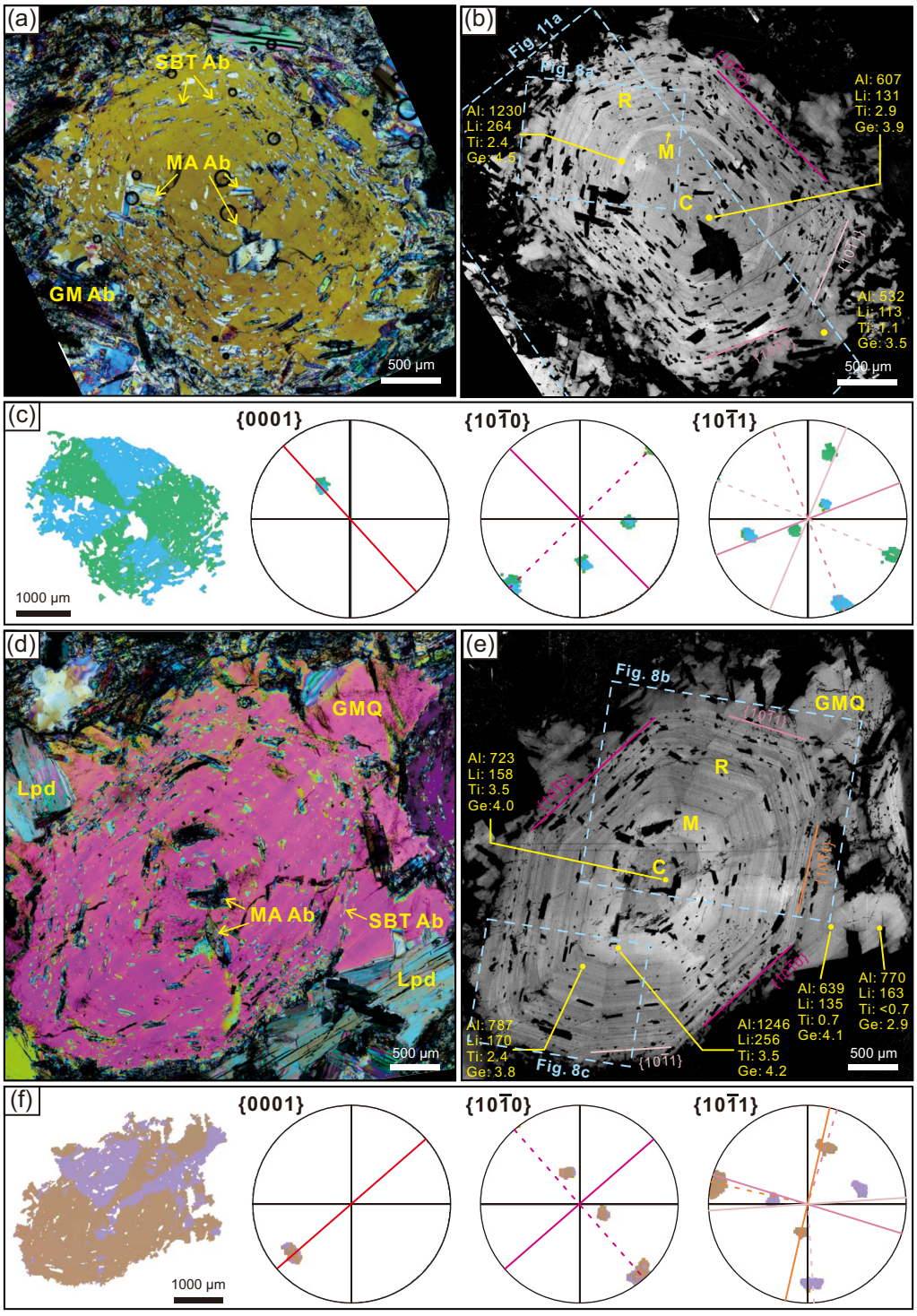

Figure 7. Photomicrographs (**a** and **d**; under crossed polarizers), CL images (**b** and **e**), and EBSD data (**c** and **f**) of representative quartz crystals from the topaz-lepidolite granite, showing the normal habit, core (C)-mantle (M)-rim (R) texture, and the Dauphiné twinning of quartz phenocrysts, and the preferential development of snowball texture on the prism faces (e.g., {10$\bar{1}$0}) of these crystals (**c**–**f**). The crystal faces of quartz, as confirmed by the EBSD pole figures, are also indicated in (**b**) and (**e**). Trace element concentrations are reported in ppm. (Color online.)

minerals (CGMs; Fig. 12g) within the same SBTQD. Similar to magmatic albite inclusions, the snowball albites have also been affected by late hydrothermal alteration (Figs. 12b–12e), particularly those located near the margins of the quartz crystals, where secondary fractures are more pronounced (Figs. 6a, 6d, 7a, 9a, and 9d).

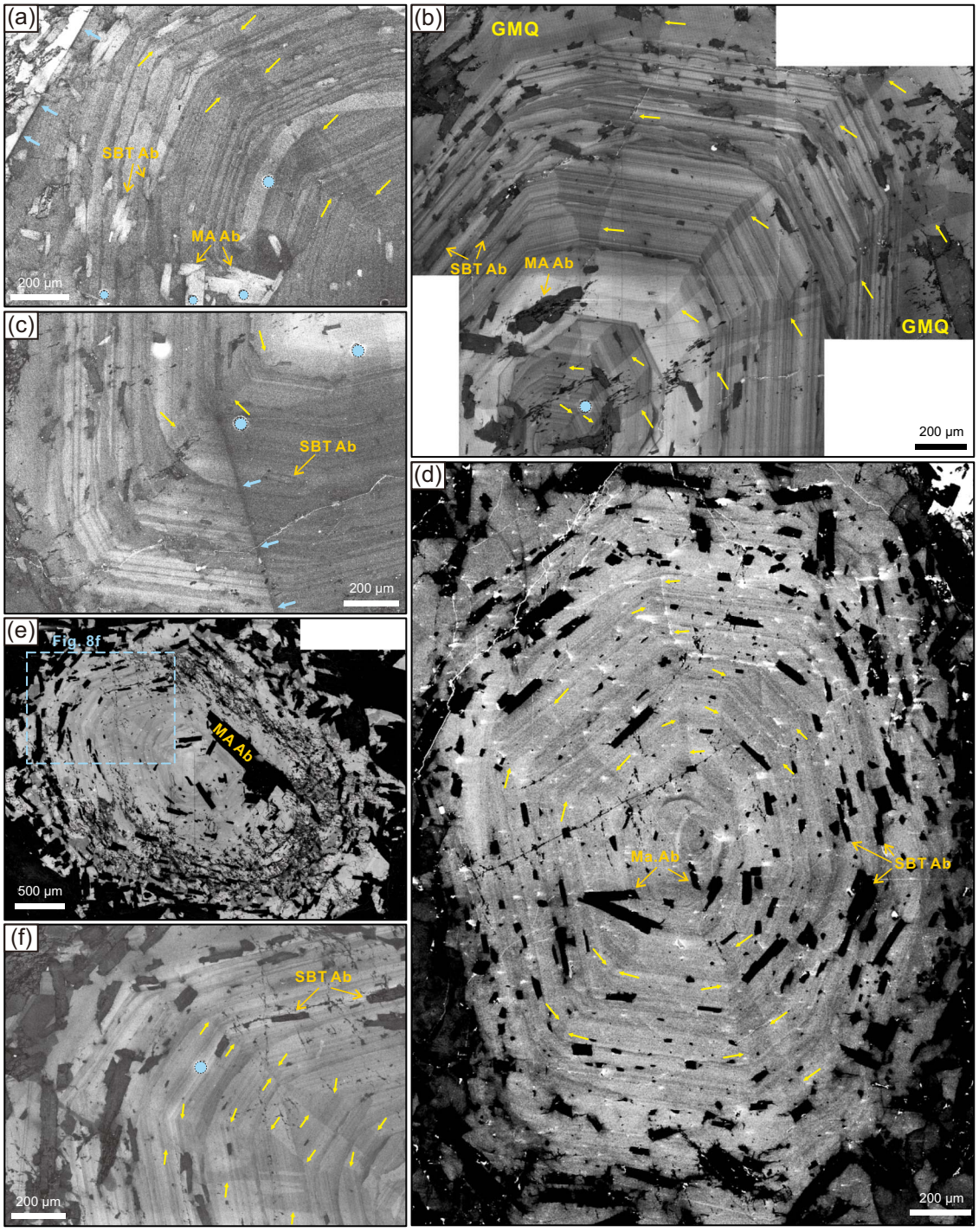

Figure 8. High-contrast CL images of specific domains of snowball quartz from topaz-lepidolite granite (**a**–**d**) and granite dike (**e**–**f**), illustrating the development of sector zoning. The yellow arrows indicate the boundaries of the sectors; the blue arrows denote the boundaries of the previous CL scan area; the blue circles represent laser ablation pits. Note that the sectors in (**b**) extend into the surrounding groundmass quartz, indicating that the sector zonation of quartz phenocryst may continue during the final paragenetic stage of growth. (Color online.)

The groundmass albites from these three granite types are larger in size compared to the other two types of albites, but they have lower aspect ratios of 2.1–3.8 (an average of 2.9; n = 12). Most of these albites are partially or completely altered; however, some fresh domains still display interference colors varying from violet, blue to bright orange (Figs. 6a, 6c, 7c, and 12h).

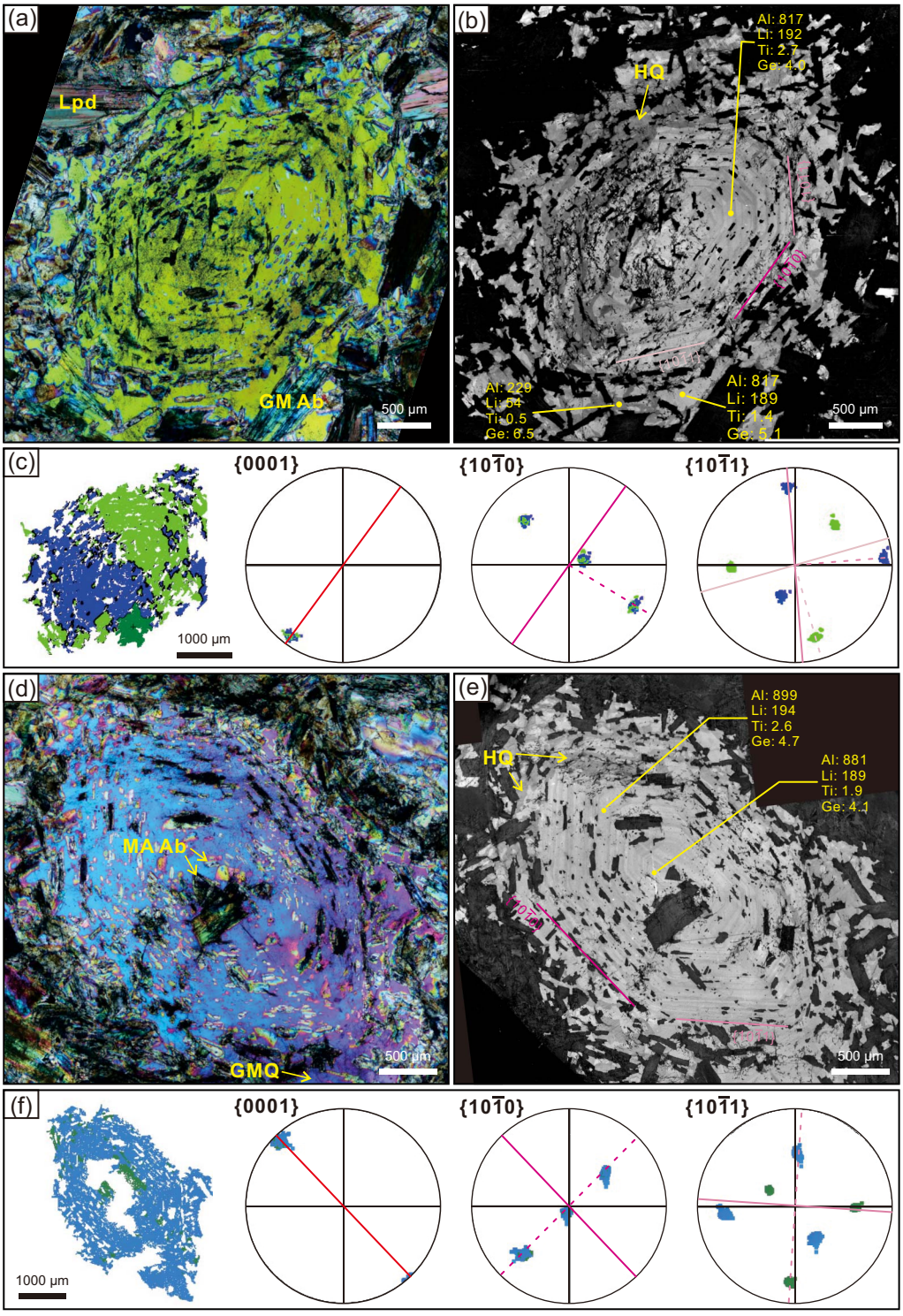

Figure 9. Photomicrographs (**a** and **d**; under crossed polarizers), CL images (**b** and **e**), and EBSD data (**c** and **f**) of typical quartz crystals from the granite dikes, showing the normal habit and Dauphiné twinning of quartz phenocrysts, the well-developed snowball texture, and significant hydrothermal alterations. The crystal faces of quartz confirmed by the EBSD are marked in (**b**) and (**e**). The concentrations (in ppm) of selected trace elements for different types of quartz crystals are also labeled in the CL images. (Color online.)

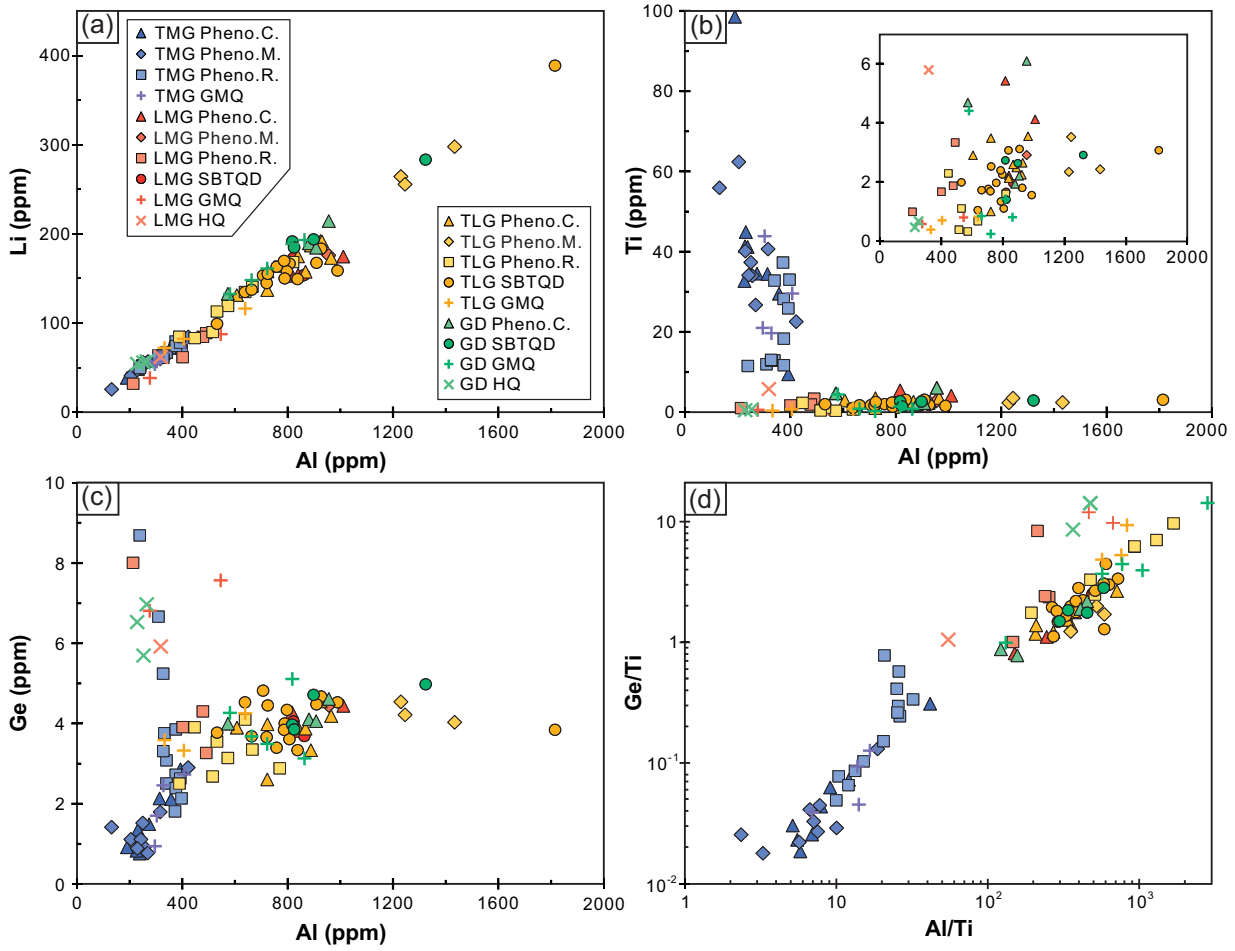

Figure 10. Trace element compositions of quartz crystals from two-mica granite (TMG), Li-mica granite (LMG), topaz-lepidolite granite (TLG), and granite dikes (GD). Abbreviations in the legend: Pheno.C. = core of quartz phenocryst; Pheno.M. = mantle of quartz phenocryst; Pheno.R. = rim of quartz phenocryst; SBTQD = snowball-textured quartz domain; GMQ = groundmass quartz; HQ = hydrothermal quartz. (Color online.)

Plagioclase chemistry

All plagioclase phenocrysts from the two-mica granite have appreciable An ($An_{3–15}$) and P_2O_5 (0.05–0.34 wt%) contents (Figs. 13a–13b). Some phenocrysts display reverse zoning, characterized by An-richer overgrowth rims or mantles (Fig. 13a; Online Materials[1] Table S2). These An-rich growth zones contain higher Sr (38–79 vs. 3–30 ppm), Pb (45–52 vs. 16–38 ppm), light rare earth element [LREE; as represented by La (3.6–5.4 vs. 0.2–4.3 ppm) and Ce (6.0–9.3 vs. 0.3–6.2 ppm)], and lower Ge (1.9–3.8 vs. 3.5–9.2 ppm) contents than the An-poor zones. The concentrations of their heavy rare earth element (HREE) and high field strength element (HFSE) are close to or below the detection limits (Online Materials[1] Table S3).

All three types of albites from Li-mica granite, topaz-lepidolite granite, and granite dikes are almost compositionally indistinguishable. They contain Ab content exceeding 97 mol% (Fig. 13a). Their P_2O_5 content ranges from 0.17 to 0.23 wt%, with traceable concentrations of Sr (≤0.8 ppm), Ba (≤0.5 ppm), Ce (<0.4 ppm), Pb (<15 ppm), and Ge (6–10 ppm) (Figs. 13b–13f). A subtle difference is that the groundmass albites tend to exhibit slightly higher Pb content (2–10 ppm) than the other two groups (primarily <5 ppm; Fig. 13e).

As illustrated in Figure 11c, the well-preserved magmatic albite inclusions and snowball albites display consistent compositional trends in Rb, Sr, and Ga. Their Rb and Ga contents steadily increase (from 0.7 to 4.7 ppm and from 32 to 40 ppm, respectively) until a drop (to 3.5 and 37 ppm, respectively) in the snowball albite that formed immediately after the CL-bright quartz mantle (Fig. 11c). In contrast, the Sr content exhibits an inverse trend, decreasing from 0.25 to 0.09 ppm and then increasing to 0.13 ppm (Fig. 11c). Nonetheless, no discernible trend can be observed in these elements for the later generations of snowball albites due to their fluctuating concentrations, which may be attributed to hydrothermal alteration, as suggested by their turbid rims (Figs. 7a and 12d–12e). Additionally, the concentrations P_2O_5 and Pb remain stable, clustering at 0.18–0.21 wt% and 2.8–3.7 ppm, respectively (Fig. 11c). Notably, the composition of the adjacent groundmass albite falls within the compositional range of these magmatic albite inclusions and snowball albites, with the exception of its slightly lower P_2O_5 content (0.15 wt%; Fig. 11c).

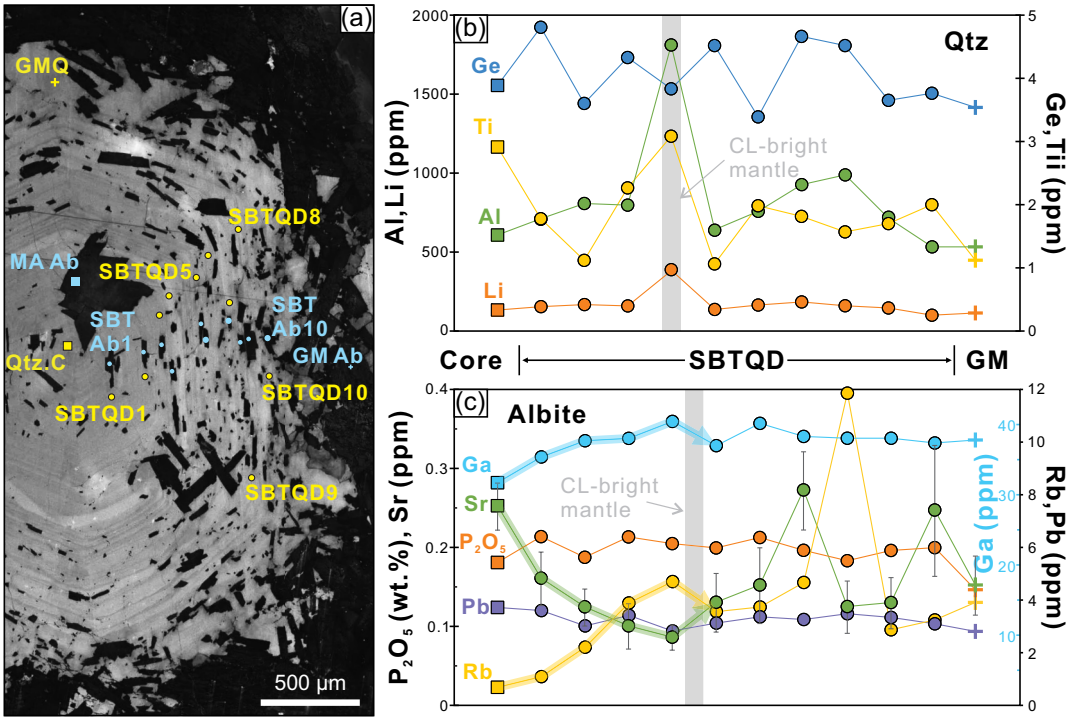

Figure 11. An integrated compositional transect of snowball quartz and albite, illustrating the chemical variations of quartz from the quartz core (Qtz.C), through the snowball-textured quartz domain (SBTQD), to the groundmass quartz (GMQ), as well as the variations of albite that are entrapped within or coexist with these quartz crystals. The symbols in (**b**) and (**c**) represent different types of albite and quartz. The filled squares denote the quartz core or the magmatic albite inclusion (MA Ab) it hosts; the filled circles represent the SBTQD or snowball albite (SBT Ab); and the crosses represent groundmass quartz or albite (GM Ab). The size of these symbols varies depending on the laser beam size used during trace element analysis, which ranged from 44 to 22 μm. Error bars are included for Rb (which are too small to be covered by the data symbols) and Sr to indicate the uncertainties in their concentrations. (Color online.)

Crystal orientation of snowball albites in quartz

The crystal orientation of snowball albites within quartz was examined from a euhedral phenocryst found in topaz-lepidolite granite (Fig. 14). This quartz exhibits a normal habit and displays oscillatory zoning (Figs. 14a–14b). The snowball albites are preferentially developed on the side adjacent to one of the prism faces (Figs. 14a–14e). As revealed by the EBSD maps, this quartz phenocryst exhibits Dauphiné twinning (Fig. 14d). However, this twinning does not disrupt the zonal distribution of snowball albites (Figs. 14d and 14g). Most snowball albites show more than two colors in the EBSD Euler map (Figs. 14d and 14g–14h), indicating the presence of several individual crystals within each albite grain (e.g., Xu et al. 2016). Their {010} face is preferentially oriented parallel to the growth zones of quartz (Figs. 14f and 14j).

Discussion

Existence of two independent magma chambers

Two different magma evolution processes have been proposed for the formation of the Yashan composite pluton. Most studies suggest that the various rock units of this pluton were emplaced successively from a deep magma chamber (Li et al. 2015; Yin et al. 1995, 2022). In contrast, Pollard (2021) interpreted the topaz-lepidolite granite as the residual melt of the Li-mica granite, which was segregated and accumulated at the roof of the latter. In both cases, these studies agree that all rock lithologies within the Yashan pluton are co-magmatic and originated from the same magma chamber. However, this perspective is challenged by the textural and chemical evidence from quartz and plagioclase presented in this study.

The quartz and plagioclase from two-mica granite exhibit distinct textural and compositional characteristics compared to those found in the other three granite types. The quartz phenocrysts in this rock display clear step zoning (Figs. 5b and 5d). Each growth zone, with the exception of the quartz rim, is texturally homogeneous and features a rounded or wavy surface, while the outer zone exhibits either higher or lower CL intensity (Figs. 5b and 5d). This complex texture suggests periodic fluctuations in melt composition and/or temperature, leading to the repetitive resorption of earlier generations of quartz (e.g., Breiter et al. 2019; Müller et al. 2009). However, such textures are rarely observed in quartz from other rocks. Furthermore, the quartz grains from this granite possess significantly higher Ti content and lower Ge/Ti and Al/Ti ratios than those from the other rocks (Figs. 10b and 10d), indicating a much less evolved nature of the two-mica granite (e.g., Breiter et al. 2019; Götze et al. 2021; Keyser et al. 2023). More importantly, there is a clear compositional gap in Ge/Ti and Al/Ti ratios between quartz crystals from the two-mica granite and those from the other rocks (Fig. 10d). Likewise, plagioclases in this rock also exhibit

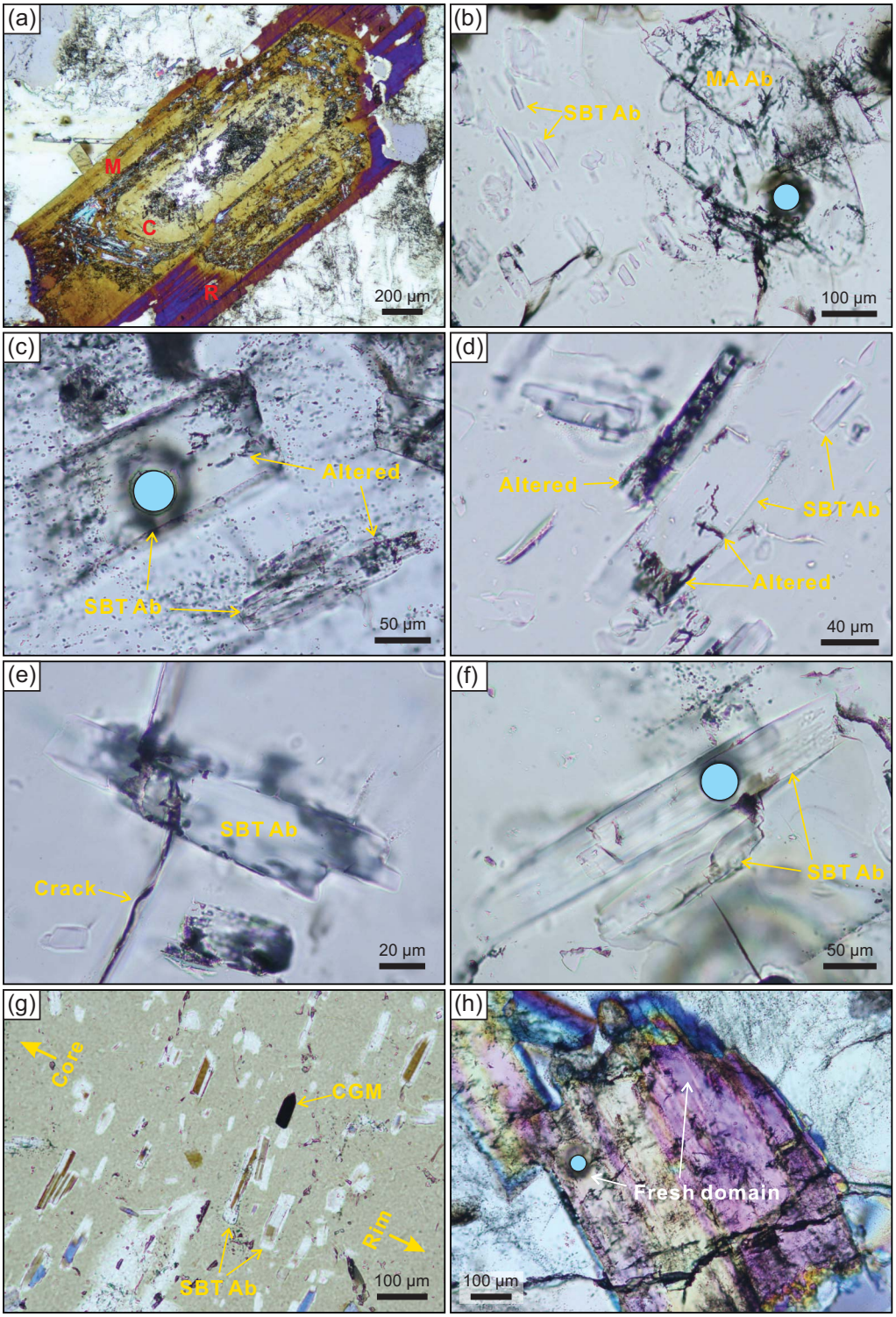

Figure 12. Photomicrographs of plagioclase in various granite types. (**a**) Plagioclase phenocryst from the two-mica granite, showing the core (C)-mantle (M)-rim (R) texture. (**b**) Partly altered magmatic albite inclusion (MA Ab) and several fresh snowball albites (SBT Ab) in quartz from the topaz-lepidolite granite. (**c**) Partly to strongly altered snowball albites in quartz from the Li-mica granite. (**d**–**e**) Variably altered snowball albites in quartz from the topaz-lepidolite granite. (**f**) Nearly fresh snowball albite in quartz from the granite dikes. (**g**) A columbite group mineral (CGM; containing 21.1 wt% Ta_2O_5, 58.8 wt% Nb_2O_5, and 18.7 wt% MnO, as revealed by EDS analysis) coexisting with snowball albites in quartz from the topaz-lepidolite granite. (**h**) Partly altered groundmass albite from the Li-mica granite. The blue circles indicate the laser ablation pits (ranging from 34 to 44 μm) on the fresh domains of albites. (Color online.)

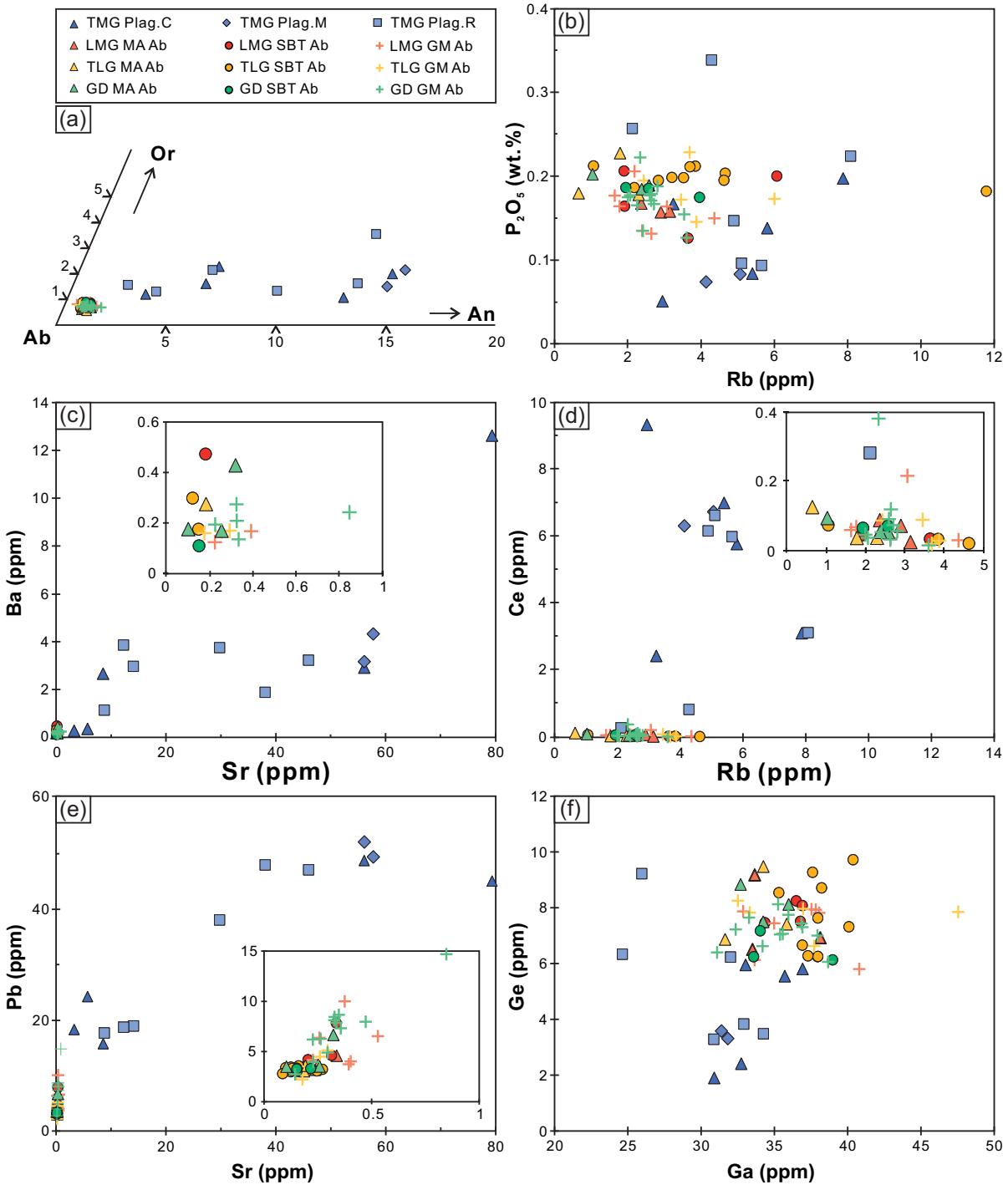

Figure 13. Ab-An-Or diagram (**a**) and trace element compositions (**b**–**f**) of plagioclase from different rocks in the Yashan pluton. Abbreviations in the legend: Plag.C. = core of plagioclase phenocryst; Plag.M. = mantle of plagioclase phenocryst; Plag.R. = rim of plagioclase phenocryst; MA Ab = magmatic albite inclusion; SBT Ab = snowball albite; GM Ab = groundmass albite. (Color online.)

complex zoning (either normal or reverse; Figs. 2a, 3a, 12a, and 13a). They contain significantly higher An content and higher Sr, Ba, La, Ce, and Pb concentrations than magmatic plagioclases (e.g., albite inclusions within quartz core) from the other three granite types (Fig. 13). These textural and chemical distinctions in quartz and plagioclase strongly suggest that the two-mica granite was derived from a different magma chamber than the one(s) that produced the other three granite types. Otherwise, at least some compositional overlap of these minerals would be expected; for instance, early generations of quartz and

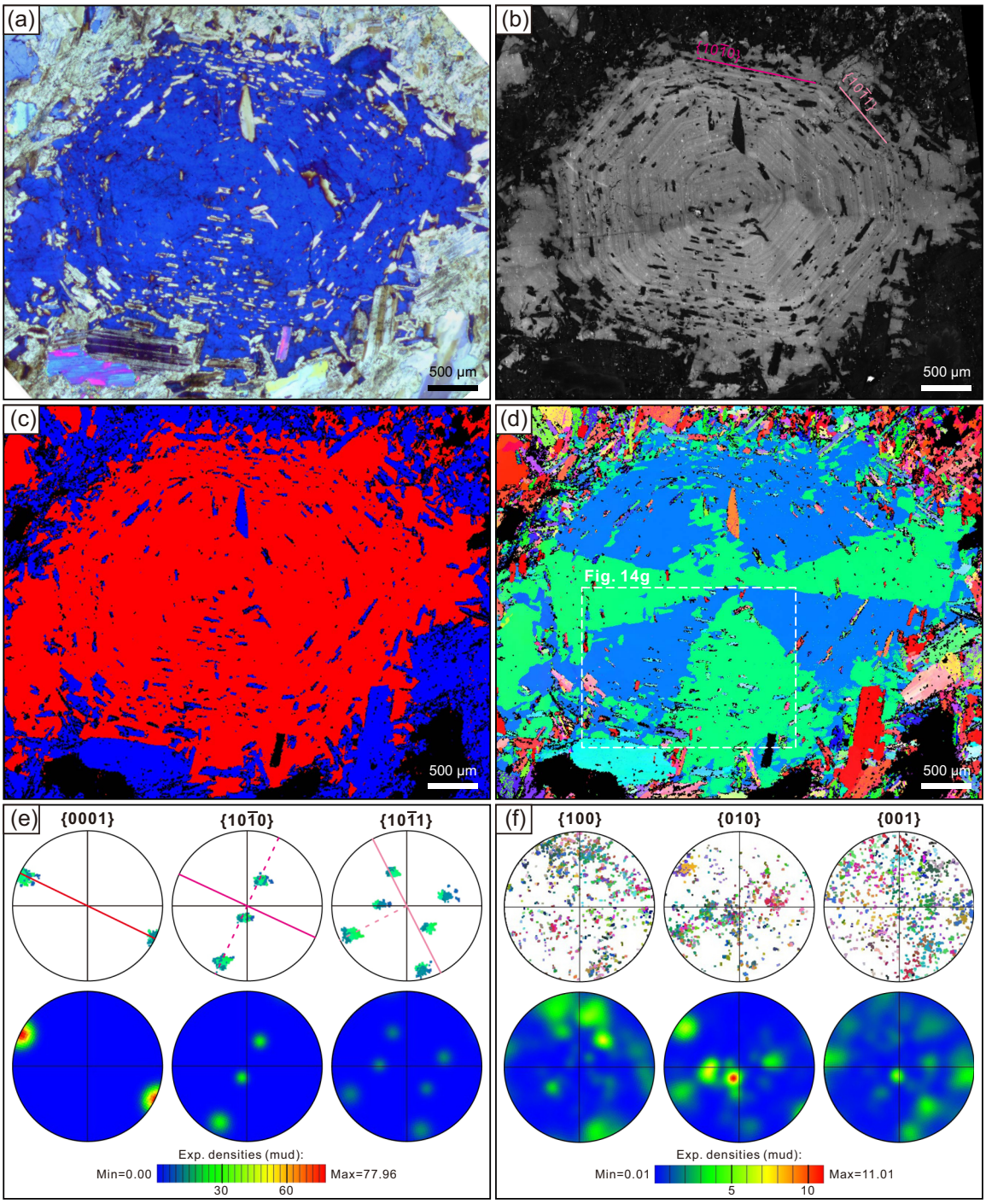

Figure 14. Photomicrograph (**a**; under crossed polarizers), CL image (**b**), and EBSD maps (**c**–**j**) of a representative quartz phenocryst from the topaz-lepidolite granite, illustrating the crystal orientation of snowball albites within quartz. (**c**) EBSD phase map of the quartz phenocryst, showing the distribution of albites (blue) within quartz (red). (**d**) EBSD Euler map of quartz and albite, showing the orientation of albites; each color represents a different orientation. Pole figures of the crystal plane orientation of quartz (**e**) and albite (**f**), along with the corresponding distribution of 2–15° orientation difference in the sample coordinate system. (**g**) Band contrast map overlaid with Euler map of quartz and albite in a selected area in (**d**). (**h**) Band contrast map overlaid with Euler map of albites in (**g**). Pole figures of the crystal plane orientation of quartz (**i**) and albite (**j**) for (**g**) and (**h**), respectively. (Color online.)

plagioclase (e.g., cognate antecrysts) would likely be recycled into or captured by later magmas (e.g., Breiter et al. 1997; Streck 2008; Zhang et al. 2022b).

The Li-mica granite, topaz-lepidolite granite, and granite dikes likely originated from a separate magma chamber. All quartz phenocrysts from these rocks exhibit oscillatory zoning

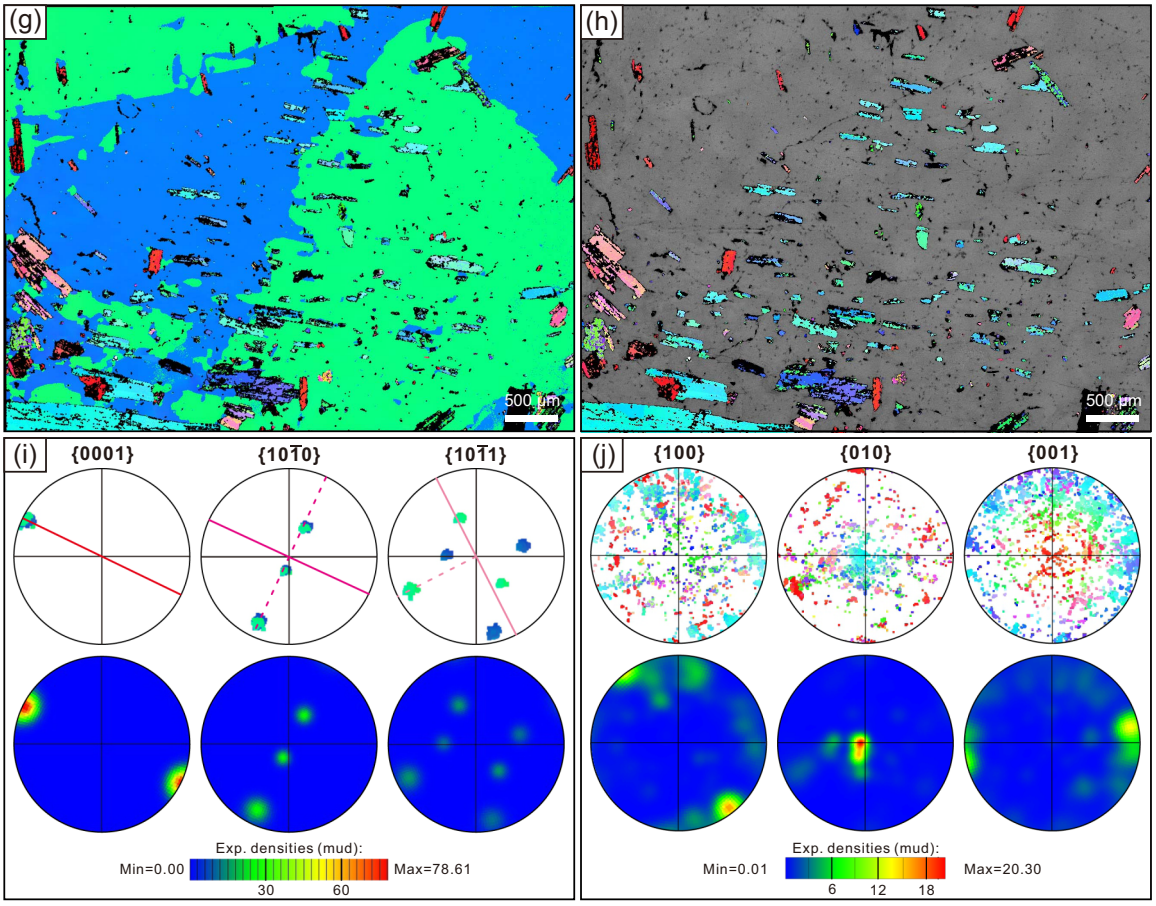

Figure 14. (*Continued.*)

(Figs. 6–9) and possess similar trace element compositions (Fig. 10). Furthermore, the quartz rims from these rocks have lower Li and Al contents than the quartz cores (Fig. 10a). This observation contradicts the general trend of increasing Li and Al concentrations during the differentiation of peraluminous granitic magma, which was driven by the crystallization of quartz and feldspars (Breiter et al. 2019; Garate-Olave et al. 2017; Müller et al. 2018). The decrease in Li content in quartz from these rocks is most likely a result of the crystallization of Li-rich minerals [e.g., Li-mica and lepidolite; Yin et al. (2022); Figs. 2b–2d and 3b–3d] from the surrounding melt (e.g., Breiter et al. 2019). As a charge-balancing element for Al ($Al^{3+} + Li^{+} \leftrightarrow Si^{4+}$), the reduction in Li would impede the incorporation of Al into the lattice of quartz crystals (Breiter et al. 2017; Götze et al. 2021). This evidence suggests that all these rocks share similar Li-rich crystallizing phases. In addition, all magmatic plagioclase inclusions entrapped within quartz cores are pure albites and are chemically similar to one another (Fig. 13). These findings indicate that these rocks were sourced from the same Li-rich magma chamber.

Slight textural differences also exist in the quartz from these rocks. The CL-bright, homogeneous mantles have been observed in quartz phenocrysts from both Li-mica granite and topaz-lepidolite granite (Figs. 6b, 7b, and 7d). The quartz mantle from Li-mica granite exhibits higher Li and Al, but lower Ti contents than the oscillatory core (Fig. 6b), which may indicate a high degree of fractionation and/or a change in growth dynamics (Breiter et al. 2019; Keyser et al. 2023; Müller et al. 2009; Wiebe et al. 2007). In contrast, the thin mantle layer of quartz from the topaz-lepidolite granite not only has much higher Al and Li but also has higher Ti contents than the quartz core (Fig. 11b), suggesting a recharge from a hotter melt (e.g., Müller et al. 2009; Wiebe et al. 2007). This observation is consistent with the resorbed surface of the quartz core (Figs. 7b and 11a). These findings indicate that topaz-lepidolite granite cannot simply be the residual melt directly separated from the parental magma of Li-mica granite, as proposed by Pollard (2021). Instead, it appears to have been emplaced later, after the magma chamber was replenished by a new batch of hot magma.

On the other hand, the rims of quartz phenocrysts from Li-mica granite, topaz-lepidolite granite, and granite dikes show varying CL intensities compared to their cores and/or mantles. The quartz rims from topaz-lepidolite granite and granite dikes display similar CL intensities to their cores and/or mantles (Figs. 7 and 9), whereas the quartz rims from Li-mica granite are much weaker than their interiors (Figs. 6b and 6e). Additionally, quartz crystals from Li-mica granite and granite dikes have been variably altered by late aqueous fluid(s) (Figs. 6 and 9), a phenomenon that is absent in quartz from topaz-lepidolite granite (Fig. 7). Different degrees of hydrothermal overprint have also been observed in cassiterites from these rocks (Zhang et al. in revision). Hydrothermal cassiterites are prevalent in Li-mica granite and granite dikes, with at least four and two generations of hydrothermal cassiterites identified in these two rocks, respectively (Zhang et al. in revision). In contrast, hydrothermal cassiterite is quite rare in topaz-lepidolite granite, with only one type observed (Zhang et al. in revision). These lines of evidence suggest that Li-mica granite, topaz-lepidolite granite, and granite dikes underwent distinct magmatic-hydrothermal evolution following their emplacement.

It can therefore be summarized that two separate magma systems were involved in the formation of the Yashan pluton. According to the different Ti content in quartz, which is sensitive to magma temperature and pressure (Huang and Audétat 2012), the two-mica granite was most probably derived from a deeper magma chamber than the one that sequentially produced Li-mica granite, topaz-lepidolite granite, and granite dikes.

Note that our conclusions regarding the two magma chambers differ from analogous studies on quartz from other composite plutons associated with rare metal deposits, i.e., the Orlovka Ta-Li deposit in Russia (Breiter et al. 2019) and the Cínovec/Zinnwald Sn-W-Li deposit in the Czech Republic (Breiter et al. 2017). In these studies, the least evolved biotite-bearing granite is considered to be comagmatic with the more evolved varieties. In the case of the Orlovka pluton, the composition of quartz from biotite granite partially overlaps with that from the evolved Li-mica granite (Breiter et al. 2019). This observation contrasts with the compositional gap noted in the Yashan pluton. One potential explanation for this discrepancy probably may stem from the limited number of samples investigated for each rock type in our study. However, a similar investigation of quartz in the vertically zoned Beauvoir pluton in France has demonstrated that quartz crystals collected from various depths within the same granite unit are chemically indistinguishable (Monnier et al. 2018). This indicates that, despite the limited number of quartz samples in our study, they could still provide comprehensive information regarding the evolution of the Yashan pluton. In addition, the Beauvoir pluton also seems to be linked to two distinct magma chambers (Cuney et al. 1992; Monnier et al. 2018). The quartz and bulk rock samples from the two-mica granite of this pluton are compositionally different from those of other granites, which cannot be solely attributed to simple fractional crystallization (Cuney et al. 1992; Monnier et al. 2018). In this case, the quartz from the two-mica granite began to crystallize at a greater depth than that from other rock types (Monnier et al. 2018). Given the increasing evidence that reveals the existence of multilevel storage zones in mature transcrustal magma systems (Cashman et al. 2017; Edmonds et al. 2019; Sparks et al. 2019), the presence of two magma chambers beneath the rare-metal granite pluton appears to be plausible.

Magmatic origin of snowball quartz

Both magmatic (Müller and Seltmann 1999; Pollard 2021; Wang et al. 2019) and metasomatic (Wu et al. 2017, 2018) origins have been proposed for snowball quartz. Major arguments supporting its metasomatic origin include: (1) the disequilibrium boundary between snowball quartz and both snowball and groundmass albites; (2) higher Ge/Ti and Al/Ti ratios in snowball quartz compared to interstitial quartz; and (3) the nearly end-member nature of snowball albite (e.g., $An_{0.3–1.1}$) (Wu et al. 2017, 2018). However, no disequilibrium boundary has been identified, as the SBTQDs generally exhibit the same oscillatory or growth zoning patterns (Figs. 6–9) and display similar crystal orientations (Figs. 7c, 7f, 9c, 9f, 14d, and 14g) as the neighboring domains without albite inclusions. Moreover, most SBTQDs are compositionally similar to the quartz cores (Fig. 10), and all of them have very low Ge/Al ratios (<0.008; Online Materials[1] Table S1). This evidence suggests that they are magmatic in origin (e.g., Müller et al. 2018). Additionally, the SBTQDs are less differentiated than groundmass quartz in the Yashan pluton, as indicated by their overall higher Al and Ti contents, lower Ge concentrations, and lower Ge/Ti and Al/Ti ratios (Fig. 10) (Breiter et al. 2017; Garate-Olave et al. 2017; Jacamon and Larsen 2009; Müller et al. 2009). This observation is expected in an evolving magma driven by the fractional crystallization of K-feldspar, plagioclase, and quartz (Pollard 2021; Yin et al. 2022). However, this trend contrasts with that of decreasing ratios of Ge/Ti and Al/Ti from snowball quartz to interstitial quartz as observed in snowball quartz within the Dajishan granite (Wu et al. 2017). One potential explanation for this discrepancy is that their groundmass quartz grains may have been affected by late hydrothermal alteration, which could have modified the original composition of the quartz. As shown in Figures 6 and 9, hydrothermal quartz is very common in Li-mica granite and granite dikes, exhibiting contrasting Ti concentrations (Fig. 4b), which probably result from their different growth rates (e.g., Huang and Audétat 2012). In the case of Li-mica granite, the hydrothermal quartz displays significantly lower Ge/Ti and Al/Ti ratios than the SBTQDs (Fig. 10d), aligning with the compositional trend observed in the Dajishan granite (Wu et al. 2017). Nonetheless, further research is necessary to validate this assumption, as the corresponding CL images are absent in Wu et al. (2017).

The chemical compositions of snowball albites further support the magmatic origin of snowball quartz. All snowball albites analyzed in this study were either well-preserved crystals (e.g., Figs. 11a and 12f) or fresh domains located away from microcracks (Fig. 12c), thereby precluding the possibility of them being equilibrated albites (e.g., Kontak 2006; Pfister et al. 2023). Consequently, their initial composition could be preserved. All snowball albites exhibit extremely low CaO (≤0.25 wt%) and traceable Sr (<0.4 ppm) contents (Figs. 13a and 13c), which compositionally contrast with hydrothermal albites (e.g., Hövelmann et al. 2010; Schwartz 1992). In contrast, they are compositionally similar to the magmatic albite inclusions found within quartz cores (Fig. 13), indicating their magmatic

origin. This interpretation is further supported by the observation that snowball albites from topaz-lepidolite granite appear to record fractional crystallization and magma mixing within the system. As illustrated in the compositional transect (Fig. 11c), well-preserved albites within the quartz core show a systematic increase in Rb and Ga, accompanied by a decrease in Sr, which is consistent with the fractional crystallization of quartz, plagioclase, and K-feldspar in this granite (Yin et al. 2022). Moreover, the concentration of these elements in the albite that formed immediately after the CL-brighter mantle decreases or increases accordingly (Fig. 11c), which aligns with mixing with a less evolved melt. Therefore, the compositional variation of snowball albites reflects the evolution of magma, confirming their magmatic origin. Nearly pure albite can indeed crystallize from the highly evolved F-rich peraluminous granitic melt under near-solidus conditions, particularly in a depression-induced undercooling environment (Lukkari and Holtz 2007; Moschini et al. 2023; Xiong et al. 1999). The F-rich character of topaz-lepidolite granite is evidenced by the high bulk rock F content (1.24–2.17 wt%; Pollard 2021) and the presence of topaz phenocryst, indicating that the F content in the melt exceeded 2.5 wt% during crystallization (Lukkari and Holtz 2007).

Snowball quartz as a result of multiple magma degassing

Since snowball quartz has been determined to be of magmatic origin, it is worthwhile to investigate further the magmatic process(es) that could account for its formation. The proposed processes include simple fractional crystallization (Pollard 2021; Yin et al. 1995) and magma degassing (Müller and Seltmann 1999; Wang et al. 2019). The snowball texture has also been observed in coexisting K-feldspar and topaz within the Yashan topaz-lepidolite granite, where abundant albite and rare lepidolite outline the growth zones of these two minerals (Pollard 2021; Yin et al. 1995). This texture is therefore suggested to have formed through the simultaneous crystallization of these minerals (Pollard 2021; Yin et al. 1995). This interpretation appears plausible, as all these phases could crystallize under near-solidus conditions in a F-rich peraluminous granitic melt (Lukkari and Holtz 2007; Xiong et al. 1999). In this scenario, albites are expected to be randomly distributed within the host minerals, similar to the distribution of magmatic albite inclusions in quartz cores (e.g., Figs. 6a, 7a, and 7d). However, this contradicts the zonal alignment of snowball albites. Furthermore, compared to magmatic albite inclusions, snowball albites commonly exhibit peculiar crystal morphology, characterized by small, prismatic shapes with high aspect ratios (mainly in a range of 5–10; Figs. 6–9). These unusual features of snowball albites, along with their greater abundance compared to scattered magmatic albite inclusions, suggest that they cannot be formed through normal crystallization but rather through rapid growth (Fenn 1977; Lofgren 1974).

The prismatic shape is the diagnostic morphology of plagioclase that formed rapidly under moderate undercooling (ΔT = 50–100 °C; the difference between the temperature of theoretical liquidus and the temperature at which crystallization initiated) of granitic melt (Fenn 1977; Rusiecka and Baker 2021; Shea and Hammer 2013). This level of undercooling is essential for the formation of the USTs in the stockscheider from the margin of topaz-lepidolite granite (Bain et al. 2022; London 2014; McCarthy and Müntener 2016). At this degree of undercooling (ΔT = 50–100 °C), quartz crystals also crystallize rapidly, transitioning from polyhedral to skeletal morphology, which results in hollow crystal faces with terraced or hopper cavities (Barbee et al. 2020; MacLellan and Trembath 1991). These terraces can range from tens to hundreds of micrometers in width, with their steps aligned parallel to the crystal face (Barbee et al. 2020). These hollow cavities serve as optimal sites for entrapping either melt or mineral inclusions during the subsequent growth of quartz, which preferentially infill on rhombohedral faces (*r* and *z*) relative to prism faces (*m*), leading to a higher number of inclusions on the prism faces (Barbee et al. 2020). This rapid skeletal growth is evidenced by the presence of sector zoning (Fig. 8), a feature characteristic of non-equilibrium growth in a fluid or fluid-rich melt (Vasyukova et al. 2013), and the preferential development of prism faces in quartz phenocrysts from the topaz-lepidolite granite and granite dikes (e.g., Barbee et al. 2020; MacLellan and Trembath 1991), where the snowball texture is well developed (Figs. 2, 7, 9, and 14). Given the specific growth habits of quartz and albite, it is suggested that abundant prismatic albites were entrapped within stair-like terraced cavities on the crystal faces of quartz during the moderate undercooling of granitic melt. This hypothesis effectively explains their preferential development on quartz prism faces (Figs. 7a–7b, 9d–9e, and 14a–14e), the zonal arrangement of snowball albites along the growth zones of quartz, and the rare instances of albites penetrating the growth zones of SBTQDs (Figs. 7b, 8d, 9e, and 14b). Where prism faces are not developed, a weak snowball texture may form on rapidly growing rhombohedral face(s) in subhedral quartz crystals (Figs. 6a–6b). Furthermore, the formation of snowball quartz was likely facilitated by local magmatic flow, which could rotate the {010} face of albite parallel to the crystal faces of quartz (Müller et al. 2011), as revealed by the EBSD pole figures.

The undercooling of magma can occur due to either a rapid decrease in melt temperature or an increase in liquidus temperature (Ubide et al. 2021). The former may happen when magma was emplaced in contact with cold country rocks, while the latter occurs during magma degassing, which can also lower the magma temperature (Černý et al. 2005; Ubide et al. 2021). Given the repetitive occurrence and compositional trend of snowball albites (Fig. 11c), it is likely that this undercooling occurred periodically. The snowball texture is characterized by multi-layers of albite inclusions, which in some cases start to develop from prism faces and gradually extend to all crystal faces (Figs. 7a–7b and 14a–14b). This development was accompanied by a temperature increase, as indicated by the rising Ti concentration in quartz (Fig. 11b). Furthermore, the well-preserved snowball albites exhibit systematic variations in Rb and Sr contents (Fig. 11c), suggesting that they crystallized sequentially from a continually evolving melt rather than simultaneously from a static melt. Consequently, the magma undercooling that led to the formation of the snowball texture was more likely associated with magma degassing (Müller and Seltmann 1999; Wang et al. 2019), as episodic degassing is common in volatile-rich felsic magmas that were emplaced at shallow depths (Ilanko et al. 2015;

Tamburello et al. 2013). This episodic degassing would induce fluctuations in pressure (and temperature) within the magma system, resulting in repeated switches from the expansion of the quartz field to the albite field [e.g., "swing eutectic" proposed by Balashov et al. (2000)]. This is consistent with the formation of multilayer UST zones in the stockscheider (Breiter et al. 2005). The development of multiple layers of unidirectional solidification textures has also been reported in the roof zones of many rare metal granites (e.g., Breiter et al. 2005; Michaud and Pichavant 2020) and porphyry systems (e.g., Bain et al. 2022; Müller et al. 2023; Kirkham and Sinclair 1988), suggesting that periodic degassing is not uncommon in such environments. In this context, the exsolved fluids were sourced not only from the topaz-lepidolite granite itself but also from the underlying magma chamber (e.g., Lowenstern and Sinclair 1996). Therefore, the formation of snowball quartz is interpreted as a consequence of multiple episodes of magma degassing.

Implications

Magmatic origin of Ta mineralization

It is controversial whether tantalite mineralization in highly fractionated peraluminous granites occurs as a magmatic (Linnen et al. 2014; López-Moro et al. 2017; Pollard 2021; Yin et al. 2022) or metasomatic (Wu et al. 2017, 2018) process. The main argument for metasomatic enrichment of Ta is based on the metasomatic origin of snowball quartz and groundmass albite (Wu et al. 2017, 2018). These studies observed that late columbite-group minerals (CGMs; stage II), which coexist with groundmass quartz and albite in topaz-lepidolite granite, are exceptionally rich in Ta and show a compositional gap with early CGMs (stage I) that are entrapped within the "metasomatic" snowball quartz. Consequently, they proposed that the Ta-rich CGMs of stage II precipitated from a hydrosilicate liquid during late metasomatism (Wu et al. 2018). However, this study demonstrates that the snowball quartz in the Yashan pluton actually formed during the magmatic stage. Furthermore, the groundmass albite and quartz from topaz-lepidolite granite are also of magmatic origin. This is evidenced by the chemical similarity of the former to magmatic albite inclusion and snowball albite (Fig. 13), while the latter shows compositional overlap with quartz phenocryst. This observation aligns with the minimal hydrothermal alteration present in this granite (as discussed above). Therefore, it is evident that tantalite in the Yashan pluton crystallized during the magmatic stage rather than the hydrothermal stage (Belkasmi et al. 2000; Yin et al. 2022).

An indicator promoting Ta(-Nb) mineralization

The primary host of Ta-Nb mineralization in the Yashan pluton is the topaz-lepidolite granite, which contains a relatively low bulk rock Ta content (122–202 ppm) (Li and Huang 2013; Pollard 2021). Considering its high Li_2O content (0.90–2.09 wt%) (Pollard 2021), the solubility of tantalite in topaz-lepidolite granite is estimated to be around 2700–2900 ppm Ta at 600 °C (Linnen 1998) that is close to the solidus temperature of highly evolved, flux-rich granitic magma (e.g., 550–600 °C) (Linnen and Cuney 2005; Lukkari and Holtz 2007). This value is significantly higher than the bulk rock Ta content. Consequently, it is perplexing how tantalite could crystallize from this granite, given its high solubility.

As suggested by Linnen and Cuney (2005) and Linnen et al. (2014), the saturation of tantalite in granites can be achieved efficiently through two different ways. The first is to increase the Ta concentration in the melt, primarily through extensive fractional crystallization. For topaz-lepidolite granite, at least 93% fractional crystallization is required to reach the saturation threshold for tantalite, assuming that Ta is completely incompatible with other crystallizing phases. However, achieving such a high degree of fractionation is challenging, as the permeability at high crystallinity (>70–80%) would become too low to allow efficient crystal-melt segregation (Bachmann and Bergantz 2004; Wolff et al. 2015). An alternative way is to reduce the solubility of tantalite by lowering the temperature of the magma and/or its Li content, both of which exert significant control on its solubility (Linnen and Cuney 2005; Linnen et al. 2014; Van Lichtervelde et al. 2010). As demonstrated in this study, the snowball quartz formed as a result of repetitive magma undercooling at a moderate degree of about 50–100 °C. If this temperature is simply assumed to represent the decrease in magma temperature at near-solidus conditions, the solubility of tantalite estimated following Linnen (1998) would sharply decline to ~300–900 ppm Ta at 500–550 °C, which is only about 10–30% of that at 600 °C. This lower solubility can be achieved more readily (with <40–80% fractional crystallization) compared to that at 600 °C. It needs to be pointed out that the practical solubility of tantalite may be even lower than the estimated values mentioned above, if the reduction in Li content in the melt is also considered, which results from the synchronous crystallization of Li-rich micas (e.g., Breiter et al. 2007). The latter is evidenced by the presence of lepidolite in SBTQDs (Pollard 2021) and the unusual decrease in Li and Al contents from the cores to the rims of quartz (Figs. 10c and 11b).

Therefore, the undercooling of magma responsible for the formation of snowball quartz is also suggested to facilitate Ta mineralization in Yashan topaz-lepidolite granite via decreasing the solubility of tantalite by more than 70–90% at near-solidus conditions. This process may have further promoted the crystallization of columbite, which had been already saturated in this granite (Yin et al. 2022; Zhang et al. in revision), as its solubility is also significantly influenced by magma temperature and Li content (Linnen 1998). Consequently, this would lead to the supersaturation and rapid growth of both minerals during the late evolutionary stage of the magma, which agrees with their structural disorder observed in natural granites (Černý et al. 1998; Linnen 1998). Therefore, the snowball quartz could serve as an exploration indicator for Ta-Nb deposits associated with highly evolved peraluminous granites.

Acknowledgments and Funding

We thank Junyi Pan and Jianming Cui from Nanjing University for their assistance with quartz LA-ICP-MS trace element analyses, Yao Xu, Xingyu Bai, and Xingkai Zhang for their support with TIMA analyses, and Yi Zhu from Yichun Ta-Nb Industrial Company for his assistance with fieldwork. We also express our gratitude to Julie Michaud, Karel Breiter, and Jason Bennett for their thorough and constructive reviews, and to Associate Editor Andreas Ertl for handling our manuscript. This research was financially supported by the National Natural Science Foundation of China (42072093 and 92462302), the "Technology + Geoscience" Project of Jiangxi Province (2023KDG01004), and a China Scholarship Council grant.

References Cited

Abdalla, H.M. (2009) Mineralogical and geochemical characterization of beryl bearing granitoids, Eastern Desert, Egypt: Metallogenic and exploration constraints. Resource Geology, 59, 121–139, https://doi.org/10.1111/j.1751-3928.2009.00085.x.

Audétat, A., Garbe-Schönberg, D., Kronz, A., Pettke, T., Rusk, B., Donovan, J.J., and Lowers, H.A. (2015) Characterisation of a natural quartz crystal as a reference material for microanalytical determination of Ti, Al, Li, Fe, Mn, Ga and Ge. Geostandards and Geoanalytical Research, 39, 171–184, https://doi.org/10.1111/j.1751-908X.2014.00309.x.

Bachmann, O. and Bergantz, G.W. (2004) On the origin of crystal-poor rhyolites: Extracted from batholithic crystal mushes. Journal of Petrology, 45, 1565–1582, https://doi.org/10.1093/petrology/egh019.

Bain, W.M., Lecumberri-Sanchez, P., Marsh, E.E., and Steele-MacInnis, M. (2022) Fluids and melts at the magmatic-hydrothermal transition, recorded by unidirectional solidification textures at Saginaw Hill, Arizona, USA. Economic Geology and the Bulletin of the Society of Economic Geologists, 117, 1543–1571, https://doi.org/10.5382/econgeo.4952.

Balashov, V., Zaraisky, G., and Seltmann, R. (2000) Fluid-magma interaction and oscillatory phenomena during crystallization of granitic melt by accumulation and escape of water and fluorine. Petrology, 8, 505–524.

Barbee, O., Chesner, C., and Deering, C. (2020) Quartz crystals in Toba rhyolites show textures symptomatic of rapid crystallization. American Mineralogist, 105, 194–226, https://doi.org/10.2138/am-2020-6947.

Belkasmi, M., Cuney, M., Pollard, P.J., and Bastoul, A. (2000) Chemistry of the Ta-Nb-Sn-W oxide minerals from the Yichun rare metal granite (SE China): Genetic implications and comparison with Moroccan and French Hercynian examples. Mineralogical Magazine, 64, 507–523, https://doi.org/10.1180/002646100549391.

Bettencourt, J.S., Leite, W.B. Jr., Goraieb, C.L., Sparrenberger, I., Bello, R.M., and Payolla, B.L. (2005) Sn-polymetallic greisen-type deposits associated with late-stage rapakivi granites, Brazil: Fluid inclusion and stable isotope characteristics. Lithos, 80, 363–386, https://doi.org/10.1016/j.lithos.2004.03.060.

Breiter, K. and Siebel, W. (1995) Granitoids in the Rozvadov Pluton, Western Bohemia and Oberpfalz. Geologische Rundschau, 84, 506–519, https://doi.org/10.1007/s005310050021.

Breiter, K., Frýda, J., Seltmann, R., and Thomas, R. (1997) Mineralogical evidence for two magmatic stages in the evolution of an extremely fractionated P-rich rare-metal granite: The Podlesí stock, Krušné hory, Czech Republic. Journal of Petrology, 38, 1723–1739, https://doi.org/10.1093/petroj/38.12.1723.

Breiter, K., Müller, A., Leichmann, J., and Gabašová, A. (2005) Textural and chemical evolution of a fractionated granitic system: The Podlesí stock, Czech Republic. Lithos, 80, 323–345, https://doi.org/10.1016/j.lithos.2003.11.004.

Breiter, K., Škoda, R., and Uher, P. (2007) Nb-Ta-Ti-W-Sn-oxide minerals as indicators of a peraluminous P- and F-rich granitic system evolution: Podlesí, Czech Republic. Mineralogy and Petrology, 91, 225–248, https://doi.org/10.1007/s00710-007-0197-1.

Breiter, K., Ackerman, L., Svojtka, M., and Müller, A. (2013) Behavior of trace elements in quartz from plutons of different geochemical signature: A case study from the Bohemian Massif, Czech Republic. Lithos, 175–176, 54–67, https://doi.org/10.1016/j.lithos.2013.04.023.

Breiter, K., Ďurišová, J., and Dosbaba, M. (2017) Quartz chemistry—A step to understanding magmatic-hydrothermal processes in ore-bearing granites: Cínovec/Zinnwald Sn-W-Li deposit, Central Europe. Ore Geology Reviews, 90, 25–35, https://doi.org/10.1016/j.oregeorev.2017.10.013.

Breiter, K., Badanina, E., Ďurišová, J., Dosbaba, M., and Syritso, L. (2019) Chemistry of quartz – A new insight into the origin of the Orlovka Ta-Li deposit, Eastern Transbaikalia, Russia. Lithos, 348–349, 105206, https://doi.org/10.1016/j.lithos.2019.105206.

Cashman, K.V., Sparks, R.S.J., and Blundy, J.D. (2017) Vertically extensive and unstable magmatic systems: A unified view of igneous processes. Science, 355, eaag3055, https://doi.org/10.1126/science.aag3055.

Černý, P., Ercit, T.S., Wise, M.A., Chapman, R., and Buck, H.M. (1998) Compositional, structural and phase relationships in titanian ixiolite and titanian columbite-tantalite. Canadian Mineralogist, 36, 547–561.

Černý, P., Blevin, P.L., Cuney, M., and London, D. (2005) Granite-related ore deposits. In J.W. Hedenquist, J.F. H. Thompson, R.J. Goldfarb, and J.P. Richards, Eds., Economic Geology One Hundredth Anniversary Volume. Society of Economic Geologists.

Che, X., Wang, R., Wu, F., Zhu, Z., Zhang, W., Hu, H., Xie, L., Lu, J., and Zhang, D. (2019) Episodic Nb–Ta mineralisation in South China: Constraints from in situ LA-ICP-MS columbite-tantalite U-Pb dating. Ore Geology Reviews, 105, 71–85, https://doi.org/10.1016/j.oregeorev.2018.11.023.

Cuney, M., Marignac, C., and Weisbrod, A. (1992) The Beauvoir topaz-lepidolite albite granite (Massif Central, France); the disseminated magmatic Sn-Li-Ta-Nb-Be mineralization. Economic Geology and the Bulletin of the Society of Economic Geologists, 87, 1766–1794, https://doi.org/10.2113/gsecongeo.87.7.1766.

Edmonds, M., Cashman, K.V., Holness, M., and Jackson, M. (2019) Architecture and dynamics of magma reservoirs. Philosophical Transactions. Series A, Mathematical, Physical, and Engineering Sciences, 377, 20180298, https://doi.org/10.1098/rsta.2018.0298.

El-Dokouny, H.A., Watanabe, Y., Mahmoud, A.S., and Dawoud, M. (2023) Geochemistry and petrogenesis of late Neoproterozoic Nuweibi and Atawi rare metals bearing granites, central Eastern Desert, Egypt. Journal of African Earth Sciences, 206, 105023, https://doi.org/10.1016/j.jafrearsci.2023.105023.

Fenn, P.M. (1977) The nucleation and growth of alkali feldspars from hydrous melts. Canadian Mineralogist, 15, 135–161.

Gahlan, H.A., Azer, M.K., Al-Hashim, M.H., and Heikal, M.T.S. (2022) Highly evolved rare-metal bearing granite overprinted by alkali metasomatism in the Arabian Shield: A case study from the Jabal Tawlah granites. Journal of African Earth Sciences, 192, 104556, https://doi.org/10.1016/j.jafrearsci.2022.104556.

Gamal-Adeen, I., Shahien, M.G., Zayed, A.M., Bakhit, B.R., Sanislav, I.V., and Abu Sharib, A.S.A.A. (2023) Sequential deuteric and hydrothermal alterations in the Late Neoproterozoic Um Naggat rare metal-bearing granite, Central Eastern Desert, Egypt. Journal of African Earth Sciences, 203, 104932, https://doi.org/10.1016/j.jafrearsci.2023.104932.

Gao, X., Zhou, Z., Breiter, K., Mao, J., Romer, R.L., Cook, N.J., and Holtz, F. (2024) Magmatic-hydrothermal fluid evolution of the tin-polymetallic metallogenic systems from the Weilasituo ore district, Northeast China. Scientific Reports, 14, 3006, https://doi.org/10.1038/s41598-024-53579-y.

Garate-Olave, I., Müller, A., Roda-Robles, E., Gil-Crespo, P.P., and Pesquera, A. (2017) Extreme fractionation in a granite-pegmatite system documented by quartz chemistry: The case study of Tres Arroyos (Central Iberian Zone, Spain). Lithos, 286–287, 162–174, https://doi.org/10.1016/j.lithos.2017.06.009.

Götze, J., Pan, Y., and Müller, A. (2021) Mineralogy and mineral chemistry of quartz: A review. Mineralogical Magazine, 85, 639–664, https://doi.org/10.1180/mgm.2021.72.

Hövelmann, J., Putnis, A., Geisler, T., Schmidt, B.C., and Golla-Schindler, U. (2010) The replacement of plagioclase feldspars by albite: Observations from hydrothermal experiments. Contributions to Mineralogy and Petrology, 159, 43–59, https://doi.org/10.1007/s00410-009-0415-4.

Huang, R. and Audétat, A. (2012) The titanium-in-quartz (TitaniQ) thermobarometer: A critical examination and re-calibration. Geochimica et Cosmochimica Acta, 84, 75–89, https://doi.org/10.1016/j.gca.2012.01.009.

Ilanko, T., Oppenheimer, C., Burgisser, A., and Kyle, P. (2015) Cyclic degassing of Erebus volcano, Antarctica. Bulletin of Volcanology, 77, 56, https://doi.org/10.1007/s00445-015-0941-z.

Jacamon, F. and Larsen, R.B. (2009) Trace element evolution of quartz in the charnockitic Kleivan granite, SW-Norway: The Ge/Ti ratio of quartz as an index of igneous differentiation. Lithos, 107, 281–291, https://doi.org/10.1016/j.lithos.2008.10.016.

Jiang, S., Wang, W., and Su, H. (2023) Super-enrichment mechanisms of strategic critical metal deposits: Current understanding and future perspectives. Journal of Earth Science, 34, 1295–1298, https://doi.org/10.1007/s12583-023-2001-5.

Jovanovski, G., Šijakova-Ivanova, T., Boev, I., Boev, B., and Makreski, P. (2022) Intriguing minerals: Quartz and its polymorphic modifications. Chemtexts, 8, 14, https://doi.org/10.1007/s40828-022-00165-2.

Keyser, W., Müller, A., Knoll, T., Menuge, J.F., Steiner, R., Berndt, J., Hart, E., Fegan, T., and Harrop, J. (2023) Quartz chemistry of lithium pegmatites and its petrogenetic and economic implications: Examples from Wolfsberg (Austria) and Moylisha (Ireland). Chemical Geology, 630, 121507, https://doi.org/10.1016/j.chemgeo.2023.121507.

Kirkham, R.V. and Sinclair, W.D. (1988) Comb quartz layers in felsic intrusions and their relationship to porphyry deposits. In R.P. Taylor and D.F. Strong, Eds., Recent Advances in the Geology of Granite-related Mineral Deposits, 39, 50–71. The Canadian Institute of Mining and Metallurgy.

Kontak, D.J. (2006) Nature and origin of an LCT-suite pegmatite with late-stage sodium enrichment, Brazil Lake, Yarmouth County, Nova Scotia. I. Geological setting and petrology. Canadian Mineralogist, 44, 563–598, https://doi.org/10.2113/gscanmin.44.3.563.

Li, S.H. (2015) Ore-forming mechanisms and prospecting models of typical granite type rare metal deposits in south China, 178 p. Ph.D. thesis, China University of Geosciences (in Chinese with English abstract).

Li, J. and Huang, X.L. (2013) Mechanism of Ta-Nb enrichment and magmatic evolution in the Yashan granites, Jiangxi Province, South China. Yanshi Xuebao, 29, 4311–4322 (in Chinese with English abstract).

Li, J., Huang, X., He, P., Li, W., Yu, Y., and Chen, L. (2015) In situ analyses of micas in the Yashan granite, South China: Constraints on magmatic and hydrothermal evolutions of W and Ta-Nb bearing granites. Ore Geology Reviews, 65, 793–810, https://doi.org/10.1016/j.oregeorev.2014.09.028.

Linnen, R.L. (1998) The solubility of Nb-Ta-Zr-Hf-W in granitic melts with Li and Li+F: Constraints for mineralization in rare metal granites and pegmatites. Economic Geology and the Bulletin of the Society of Economic Geologists, 93, 1013–1025, https://doi.org/10.2113/gsecongeo.93.7.1013.

Linnen, R.L. and Cuney, M. (2005) Granite-related rare-element deposits and experimental constraints on Ta-Nb-W-Sn-Zr-Hf mineralization. In R.L. Linnen and I.M. Samson, Eds., Rare-element Geochemistry and Mineral Deposits, 17, 45–67. Geological Association of Canada Short Course.

Linnen, R.L., Samson, I.M., Williams-Jones, A.E., and Chakhmouradian, A.R. (2014) Geochemistry of the Rare-Earth Element, Nb, Ta, Hf, and Zr Deposits. In H.D. Holland and K.K. Turekian, Eds., Treatise on Geochemistry (2nd Edition), 13, 543–568. Elsevier.

Liu, W., Xu, H., and Shi, F. (2021) Decorated dislocations in naturally deformed olivine with C-type fabric: A case study in the Lüliangshan garnet peridotite from the North Qaidam ultrahigh-pressure belt, NW China. Tectonophysics, 814, 228971, https://doi.org/10.1016/j.tecto.2021.228971.

Lofgren, G. (1974) An experimental study of plagioclase crystal morphology; isothermal crystallization. American Journal of Science, 274, 243–273, https://doi.org/10.2475/ajs.274.3.243.

London, D. (2014) A petrologic assessment of internal zonation in granitic pegmatites. Lithos, 184–187, 74–104, https://doi.org/10.1016/j.lithos.2013.10.025.

López-Moro, F.J., García Polonio, F., Llorens González, T., Sanz Contreras, J.L., Fernández Fernández, A., and Moro Benito, M.C. (2017) Ta and Sn concentration by muscovite fractionation and degassing in a lens-like granite body: The case study of the Penouta rare-metal albite granite (NW Spain). Ore Geology Reviews, 82, 10–30, https://doi.org/10.1016/j.oregeorev.2016.11.027.

Lou, F.S., Shen, W.Z., Wang, D.Z., Shu, L.S., Wu, F.J., Zhang, F.R., and Yu, J.H. (2005) Zircon U-Pb isotopic chronology of the Wugongshan dome compound granite in Jiangxi Province. Acta Geologica Sinica, 79, 636–644 (in Chinese with English abstract).

Lowenstern, J.B. and Sinclair, W.D. (1996) Exsolved magmatic fluid and its role in the formation of comb-layered quartz at the Cretaceous Logtung W-Mo deposit, Yukon territory, Canada. Earth and Environmental Science Transactions of the Royal Society of Edinburgh, 87, 291–303, https://doi.org/10.1017/S0263593300006696.

Lukkari, S. and Holtz, F. (2007) Phase relations of a F-enriched peraluminous granite: An experimental study of the Kymi topaz granite stock, southern Finland. Contributions to Mineralogy and Petrology, 153, 273–288, https://doi.org/10.1007/s00410-006-0146-8.

MacLellan, H.E. and Trembath, L.T. (1991) The role of quartz crystallization in the development and preservation of igneous texture in granitic rocks; experimental evidence at 1 kbar. American Mineralogist, 76, 1291–1305.

Marignac, C., Cuney, M., Cathelineau, M., Lecomte, A., Carocci, E., and Pinto, F. (2020) The Panasqueira rare metal granite suites and their involvement in the genesis of the World-Class Panasqueira W-Sn-Cu vein deposit: A petrographic, mineralogical, and geochemical study. Minerals, 10, 562, https://doi.org/10.3390/min10060562.

McCarthy, A. and Müntener, O. (2016) Comb layering monitors decompressing and fractionating hydrous mafic magmas in subvolcanic plumbing systems (Fisher Lake, Sierra Nevada, USA). Journal of Geophysical Research: Solid Earth, 121, 8595–8621, https://doi.org/10.1002/2016JB013489.

Michaud, J.A.-S. and Pichavant, M. (2020) Magmatic fractionation and the magmatic-hydrothermal transition in rare metal granites: Evidence from Argemela (Central Portugal). Geochimica et Cosmochimica Acta, 289, 130–157, https://doi.org/10.1016/j.gca.2020.08.022.

Michaud, J.A.-S., Gumiaux, C., Pichavant, M., Gloaguen, E., and Marcoux, E. (2020) From magmatic to hydrothermal Sn-Li-(Nb-Ta-W) mineralization: The Argemela area (central Portugal). Ore Geology Reviews, 116, 103215, https://doi.org/10.1016/j.oregeorev.2019.103215.

Monnier, L., Lach, P., Salvi, S., Melleton, J., Bailly, L., Béziat, D., Monnier, Y., and Gouy, S. (2018) Quartz trace-element composition by LA-ICP-MS as proxy for granite differentiation, hydrothermal episodes, and related mineralization: The Beauvoir Granite (Echassières district), France. Lithos, 320–321, 355–377, https://doi.org/10.1016/j.lithos.2018.09.024.

Moschini, P., Mollo, S., Pontesilli, A., Nazzari, M., Petrone, C.M., Fanara, S., Vona, A., Gaeta, M., Romano, C., and Scarlato, P. (2023) A review of plagioclase growth rate and compositional evolution in mafic alkaline magmas: Guidelines for thermometry, hygrometry, and timescales of magma dynamics at Stromboli and Mt. Etna. Earth-Science Reviews, 240, 104399, https://doi.org/10.1016/j.earscirev.2023.104399.

Müller, A. and Seltmann, R. (1999) The genetic significance of snowball quartz in high fractionated tin granites of the Krušne Hory/Erzgebirge. Mineral Deposits. Processes to Processing, 1, 409–412.

Müller, A., Seltmann, R., and Behr, H.-J. (2000) Application of cathodoluminescence to magmatic quartz in a tin granite – case study from the Schellerhau Granite Complex, Eastern Erzgebirge, Germany. Mineralium Deposita, 35, 169–189, https://doi.org/10.1007/s001260050014.

Müller, A., van den Kerkhof, A.M., Behr, H.-J., Kronz, A., and Koch-Müller, M. (2009) The evolution of late-Hercynian granites and rhyolites documented by quartz—A review. Earth and Environmental Science Transactions of the Royal Society of Edinburgh, 100, 185–204, https://doi.org/10.1017/S1755691009016144.

Müller, A., Leiss, B., Ullemeyer, K., and Breiter, K. (2011) Lattice-preferred orientations of late-Variscan granitoids derived from neutron diffraction data: Implications for magma emplacement mechanisms. International Journal of Earth Sciences, 100, 1515–1532, https://doi.org/10.1007/s00531-010-0590-6.

Müller, A., Herklotz, G., and Giegling, H. (2018) Chemistry of quartz related to the Zinnwald/Cínovec Sn-W-Li greisen-type deposit, Eastern Erzgebirge, Germany. Journal of Geochemical Exploration, 190, 357–373, https://doi.org/10.1016/j.gexplo.2018.04.009.

Müller, A., Kirwin, D., and Seltmann, R. (2023) Textural characterization of unidirectional solidification textures related to Cu-Au deposits and their implication for metallogenesis and exploration. Mineralium Deposita, 58, 1211–1235, https://doi.org/10.1007/s00126-023-01175-x.

Pan, J., Ni, P., and Wang, R. (2019) Comparison of fluid processes in coexisting wolframite and quartz from a giant vein-type tungsten deposit, South China: Insights from detailed petrography and LA-ICP-MS analysis of fluid inclusions. American Mineralogist, 104, 1092–1116, https://doi.org/10.2138/am-2019-6958.

Pfister, J.D., Kontak, D.J., and Groat, L.A. (2023) Textural and mineralogical evolution of the Little Nahanni Pegmatite Group (NWT, Canada) with implications for metasomatism, rare-metal mineralization, and pegmatite–wall rock interaction. The Canadian Journal of Mineralogy and Petrology, 61, 467–505, https://doi.org/10.3749/2000086.

Pollard, P.J. (2021) The Yichun Ta-Sn-Li Deposit, South China: Evidence for Extreme chemical fractionation in F-Li-P-rich magma. Economic Geology and the Bulletin of the Society of Economic Geologists, 116, 453–469, https://doi.org/10.5382/econgeo.4801.

Robyr, M., Carlson, W.D., Passchier, C., and Vonlanthen, P. (2009) Microstructural, chemical and textural records during growth of snowball garnet. Journal of Metamorphic Geology, 27, 423–437, https://doi.org/10.1111/j.1525-1314.2009.00824.x.

Rusiecka, M.K. and Baker, D.R. (2021) Growth and textural evolution during crystallization of quartz and feldspar in hydrous, rhyolitic melt. Contributions to Mineralogy and Petrology, 176, 48, https://doi.org/10.1007/s00410-021-01809-1.

Schwartz, M.O. (1992) Geochemical criteria for distinguishing magmatic and metasomatic albite-enrichment in granitoids—examples from the Ta-Li Granite Yichun (China) and the Sn-W deposit Tikus (Indonesia). Mineralium Deposita, 27, 101–108, https://doi.org/10.1007/BF00197092.

Seddik, A.M.A., Darwish, M.H., Azer, M.K., and Asimow, P.D. (2020) Assessment of magmatic versus post-magmatic processes in the Mueilha rare-metal granite, Eastern Desert of Egypt, Arabian-Nubian Shield. Lithos, 366–367, 105542, https://doi.org/10.1016/j.lithos.2020.105542.

Shea, T. and Hammer, J.E. (2013) Kinetics of cooling- and decompression-induced crystallization in hydrous mafic-intermediate magmas. Journal of Volcanology and Geothermal Research, 260, 127–145, https://doi.org/10.1016/j.jvolgeores.2013.04.018.

Sirqueira, A.R.F., Moura, M.A., Botelho, N.F., and Kyser, T.K. (2018) Nature and evolution of Paleoproterozoic Sn and rare metal albitites from central Brazil: Constraints based on textural, geochemical, Ar-Ar, and oxygen isotopes. Minerals, 8, 396, https://doi.org/10.3390/min8090396.

Soloviev, S.G., Kryazhev, S., and Dvurechenskaya, S. (2020) Geology, igneous geochemistry, mineralization, and fluid inclusion characteristics of the Kougarok tin-tantalum-lithium prospect, Seward Peninsula, Alaska, USA. Mineralium Deposita, 55, 79–106, https://doi.org/10.1007/s00126-019-00883-7.

Sparks, R.S.J., Annen, C., Blundy, J.D., Cashman, K.V., Rust, A.C., and Jackson, M.D. (2019) Formation and dynamics of magma reservoirs. Philosophical Transactions of the Royal Society A, 377, 20180019, https://doi.org/10.1098/rsta.2018.0019.

Streck, M.J. (2008) Mineral textures and zoning as evidence for open system processes. Reviews in Mineralogy and Geochemistry, 69, 595–622, https://doi.org/10.2138/rmg.2008.69.15.

Sun, D., Wang, S., Gou, J., Zhang, D., Deng, C., Yang, D., and Tian, L. (2023) Petrogenesis of Shihuiyao rare-metal granites in the southern Great Xing'an Range, NE China. Minerals, 13, 701, https://doi.org/10.3390/min13050701.

Tamburello, G., Aiuppa, A., McGonigle, A.J.S., Allard, P., Cannata, A., Giudice, G., Kantzas, E.P., and Pering, T.D. (2013) Periodic volcanic degassing behavior: The Mount Etna example. Geophysical Research Letters, 40, 4818–4822, https://doi.org/10.1002/grl.50924.

Ubide, T., Neave, D.A., Petrelli, M., and Longpré, M.-A. (2021) Editorial: Crystal archives of magmatic processes. Frontiers in Earth Science (Lausanne), 9, 749100, https://doi.org/10.3389/feart.2021.749100.

Van Lichtervelde, M., Holtz, F., and Hanchar, J.M. (2010) Solubility of manganotantalite, zircon and hafnon in highly fluxed peralkaline to peraluminous pegmatitic melts. Contributions to Mineralogy and Petrology, 160, 17–32, https://doi.org/10.1007/s00410-009-0462-x.

Vasyukova, O.V., Kamenetsky, V.S., Goemann, K., and Davidson, P. (2013) Diversity of primary CL textures in quartz from porphyry environments: Implication for origin of quartz eyes. Contributions to Mineralogy and Petrology, 166, 1253–1268, https://doi.org/10.1007/s00410-013-0923-0.

Wang, D., Liu, J., Carranza, E.J.M., Zhai, D., Wang, Y., Zhen, S., Wang, J., Wang, J., Liu, Z., and Zhang, F. (2019) Formation and evolution of snowball quartz phenocrysts in the Dongping porphyritic granite, Hebei Province, China: Insights from fluid inclusions, cathodoluminescence, trace elements, and crystal size distribution study. Lithos, 340–341, 239–254, https://doi.org/10.1016/j.lithos.2019.05.018.

Wang, R., Che, X., Wu, B., and Xie, L. (2020) Critical mineral resources of Nb, Ta, Zr, and Hf in China. Kexue Tongbao, 65, 3763–3777, https://doi.org/10.1360/TB-2020-0271.

Wiebe, R.A., Wark, D.A., and Hawkins, D.P. (2007) Insights from quartz cathodoluminescence zoning into crystallization of the Vinalhaven granite, coastal Maine. Contributions to Mineralogy and Petrology, 154, 439–453, https://doi.org/10.1007/s00410-007-0202-z.

Williams, P.F. and Jiang, D. (1999) Rotating garnets. Journal of Metamorphic Geology, 17, 367–378, https://doi.org/10.1046/j.1525-1314.1999.00203.x.

Wolff, J.A., Ellis, B.S., Ramos, F.C., Starkel, W.A., Boroughs, S., Olin, P.H., and Bachmann, O. (2015) Remelting of cumulates as a process for producing chemical zoning in silicic tuffs: A comparison of cool, wet and hot, dry rhyolitic magma systems. Lithos, 236–237, 275–286, https://doi.org/10.1016/j.lithos.2015.09.002.

Wu, C., Liu, S., Gu, L., Zhang, Z., and Lei, R. (2011) Formation mechanism of the lanthanide tetrad effect for a topaz- and amazonite-bearing leucogranite pluton in eastern Xinjiang, NW China. Journal of Asian Earth Sciences, 42, 903–916, https://doi.org/10.1016/j.jseaes.2010.09.011.

Wu, M., Samson, I.M., and Zhang, D. (2017) Textural and chemical constraints on the formation of disseminated granite-hosted W-Ta-Nb mineralization at the Dajishan deposit, Nanling Range, Southeastern China. Economic Geology and the Bulletin of the Society of Economic Geologists, 112, 855–887, https://doi.org/10.2113/econgeo.112.4.855.

——— (2018) Textural features and chemical evolution in Ta-Nb oxides: Implications for deuteric rare-metal mineralization in the Yichun granite-marginal pegmatite, Southeastern China. Economic Geology and the Bulletin of the Society of Economic Geologists, 113, 937–960, https://doi.org/10.5382/econgeo.2018.4577.

Xie, L., Wang, Z., Wang, R., Zhu, J., Che, X., Gao, J., and Zhao, X. (2018) Mineralogical constraints on the genesis of W-Nb-Ta mineralization in the Laizilling granite (Xianghualing district, south China). Ore Geology Reviews, 95, 695–712, https://doi.org/10.1016/j.oregeorev.2018.03.021.

Xiong, X., Zhao, Z., Zhu, J., and Rao, B. (1999) Phase relations in albite granite-H_2O-HF system and their petrogenetic applications. Geochemical Journal, 33, 199–214, https://doi.org/10.2343/geochemj.33.199.

Xu, C., Zhao, S., Li, C., and He, X. (2016) Plagioclase twins in a basalt: An electron backscatter diffraction study. Journal of Applied Crystallography, 49, 2145–2154, https://doi.org/10.1107/S1600576716015739.

Yang, Z.L., Qiu, J.S., Xing, G.F., Yu, M., and Zhao, J. (2014) Petrogenesis and magmatic evolution of the Yashan granite pluton in Yichun, Jiangxi Province, and their constraints on mineralization. Acta Geologica Sinica, 88, 850–868 (in Chinese with English abstract).

Yin, L., Pollard, P.J., Hu, S.X., and Taylor, R.G. (1995) Geologic and geochemical characteristics of the Yichun Ta-Nb-Li Deposit, Jiangxi Province, South China. Economic Geology and the Bulletin of the Society of Economic Geologists, 90, 577–585, https://doi.org/10.2113/gsecongeo.90.3.577.

Yin, R., Huang, X., Wang, R., Sun, X., Tang, Y., Wang, Y., and Xu, Y. (2022) Rare-metal enrichment and Nb-Ta fractionation during magmatic-hydrothermal processes in rare-metal granites: Evidence from zoned micas from the Yashan Pluton, South China. Journal of Petrology, 63, egac093, https://doi.org/10.1093/petrology/egac093.

Zhang, Y., Ma, D.S., Xu, Z., Zhao, H., and Zhu, L. (2019) Molybdenite Re-Os age of Yashan 414 Ta-Li deposit and its prospecting significance. 9th National Academic Symposium on Mineralization Theory and Prospecting Methods, p. 180–181 (in Chinese).

Zhang, T., Hou, Z., Zheng, Y., Cheng, X., Wang, S., and Teng, X. (2022a) Geochronology and geochemistry of the granites from the Jiabusi Ta-Nb-(Li-Rb-Cs) deposit at the northern margin of the North China Craton. Ore Geology Reviews, 147, 104969, https://doi.org/10.1016/j.oregeorev.2022.104969.

Zhang, D., Wei, J., Nadeau, O., Shi, W., and Dan, K. (2022b) Magmatic and hydrothermal evolution at Qian'echong, Central-Eastern China: Insights into Dabie-type porphyry Mo mineralization. Journal of Petrology, 63, egac013, https://doi.org/10.1093/petrology/egac013.

Zhao, S., Xu, H., Wang, Q., and Yang, K. (2013) Electron backscatter diffraction study of twins and intergrowths among quartz crystals in granite. Journal of Applied Crystallography, 46, 1414–1424, https://doi.org/10.1107/S0021889813017913.

Zhu, J., Li, R., Li, F., Xiong, X., Zhou, F., and Huang, X. (2001) Topaz-albite granites and rare-metal mineralization in the Limu District, Guangxi Province, southeast China. Mineralium Deposita, 36, 393–405, https://doi.org/10.1007/s001260100160.

Zhu, Z., Wang, R., Li, J., Chen, Z., Wang, D., and Mercadier, J. (2024) Magmatic-hydrothermal stage recorded by mica zonation and Nb-Ta-W-Sn mineralization: New insight into the genesis of highly evolved Songshugang Nb-Ta deposit (Jiangxi, SE China). Ore Geology Reviews, 168, 106012, https://doi.org/10.1016/j.oregeorev.2024.106012.

Manuscript received October 14, 2024
Manuscript accepted February 9, 2025
Accepted manuscript online February 19, 2025
Manuscript Handled by Andreas Ertl

Endnotes:

[1]Deposit item AM-25-109649. Online Materials are free to all readers. Go online, via the table of contents or article view, and find the tab or link for supplemental materials.